

New Observations From the SWIM Radar On-Board CFOSAT: Instrument Validation and Ocean Wave Measurement Assessment

Danièle Hauser¹, Member, IEEE, Cédric Tourain², Laura Hermozo, D. Alraddawi, L. Aouf, B. Chapron, A. Dalphiné, L. Delaye, M. Dalila, E. Dormy³, F. Gouillon⁴, V. Gressani, A. Grouazel, G. Guitton, R. Husson, A. Mironov, A. Mouche⁵, A. Ollivier, L. Oruba, F. Piras, R. Rodriguez Suquet⁶, P. Schippers, C. Tison, and Ngan Tran

Abstract—This article describes the first results obtained from the Surface Waves Investigation and Monitoring (SWIM) instrument carried by the China France Oceanography Satellite (CFOSAT), which was launched on October 29, 2018. SWIM is a Ku-band radar with a near-nadir scanning beam geometry. It was designed to measure the spectral properties of surface ocean waves. First, the good behavior of the instrument is illustrated. It is then shown that the nadir products (significant wave height, normalized radar cross section, and wind speed) exhibit an accuracy similar to standard altimeter missions, thanks to a new retracking algorithm, which compensates a lower sampling rate compared to standard altimetry missions. The off-nadir beam observations are analyzed in detail. The normalized radar cross section varies with incidence and wind speed as expected from previous studies presented in the literature. We illustrate that, in order to retrieve the wave spectra from the radar backscattering fluctuations, it is crucial to apply a speckle correction derived from the observations. Directional spectra of ocean waves and their mean parameters are then compared to

wave model data at the global scale and to *in situ* data from a selection of case studies. The good efficiency of SWIM to provide the spectral properties of ocean waves in the wavelength range [70–500 m] is illustrated. The main limitations are discussed, and the perspectives to improve the data quality are presented.

Index Terms—Altimeter, ocean wave spectra, radar measurements, scatterometer, sea surface, spaceborne radar, speckle noise.

I. INTRODUCTION

SINCE October 2018, a new spaceborne system for measuring ocean surface parameters has been deployed, namely the China France Oceanography Satellite (CFOSAT) developed under the responsibilities of the French and Chinese Space agencies [the Centre National d'Etudes Spatiales (CNES), the Chinese National Space Agency (CNSA), and the National Satellite Oceanic Application Service (NSOAS)]. This satellite was designed to monitor, at the global scale, ocean surface winds and waves so as to improve the wind and wave forecast for marine meteorology (including severe events), ocean dynamics modeling and prediction, climate variability knowledge, fundamental knowledge of surface processes. CFOSAT also offers an opportunity to complement other satellite missions for the estimation of land surface parameters (in particular soil moisture and soil roughness) and polar ice sheet characteristics. The main objectives and characteristics were already presented in [1] and [2].

This mission is a very innovative one, for several reasons. First, thanks to its near-nadir scatterometer Surface Waves Investigation and Monitoring (SWIM), it is the first time that directional spectra of ocean waves are produced systematically with a real-aperture scanning radar system. With this concept, the backscattered signal is sampled with a high horizontal resolution of only a few meters in the range direction but averaged over a large footprint (several kilometers) in the perpendicular direction. Hence, waves with a significant component in the azimuth direction are averaged over many wavelengths and, therefore, contribute little to the radar signal. Only long waves traveling in the range direction will be seen because of the sensitivity of the radar backscatter to the local tilting of the surface. Their direction is determined from the known pointing direction of the antenna and from its rotating capability insuring a 360° detection. This concept is a useful

Manuscript received October 16, 2019; revised February 20, 2020 and April 21, 2020; accepted April 30, 2020. Date of publication June 1, 2020; date of current version December 24, 2020. This work was supported by the Centre National d'Etude Spatiales (CNES), Toulouse, France. (Corresponding author: Danièle Hauser.)

Danièle Hauser, D. Alraddawi, and L. Oruba are with the LATMOS, Université Paris-Saclay, UVSQ, CNRS, Sorbonne Université, 78280 Guyancourt, France (e-mail: danièle.hauser@latmos.ipsl.fr).

Cédric Tourain, Laura Hermozo, F. Gouillon, R. Rodriguez Suquet, and C. Tison are with the Centre National d'Etudes Spatiales, 31400 Toulouse, France (e-mail: cedric.tourain@cnes.fr).

L. Aouf and A. Dalphiné are with the Division of Marine and Oceanography, Météo-France, 31100 Toulouse, France (e-mail: lotfi.aouf@meteo.fr).

B. Chapron, A. Grouazel, and A. Mouche are with Laboratoire Océanographie Physique et Spatiale (LOPS), Ifremer, 29280 Plouzané, France (e-mail: bchapron@ifremer.fr).

L. Delaye was with ACRI-ST, 78280 Guyancourt, France. She is now with the Institut National de la Propriété Industrielle, 92677 Courbevoie, France.

M. Dalila, R. Husson, A. Ollivier, F. Piras, and Ngan Tran are with Collecte Localisation Satellites, 31520 Ramonville Saint-Agne, France (e-mail: aollivier@grouplcs.com).

E. Dormy is with Ecole Normale Supérieure, 75005 Paris, France (e-mail: dormy@dma.ens.fr).

V. Gressani is with Ifremer, 29280 Plouzané, France.

G. Guitton is with Oceandatalab, 29280 Locmaria-Plouzané, France (e-mail: gilles.guitton@oceandatalab.com).

A. Mironov is with Eodyn, 29280 Plouzané, France (e-mail: alexey.mironov@eodyn.com).

P. Schippers is with ACRI-ST, 78280 Guyancourt, France (e-mail: patricia.schippers@acri-st.fr).

Color versions of one or more of the figures in this article are available online at <https://ieeexplore.ieee.org>.

Digital Object Identifier 10.1109/TGRS.2020.2994372

0196-2892 © 2020 IEEE. Personal use is permitted, but republication/redistribution requires IEEE permission.

See <https://www.ieee.org/publications/rights/index.html> for more information.

complement to synthetic aperture radar (SAR) observations which are also used to provide wave spectra over the ocean but with frequent smearing effects, for waves shorter than about 200 m propagating with a component in the along-track directions [3], even if recent results by Li *et al.* [4] show that it is possible to extract consistent information on wind waves from waves propagation across-track. Second, the mission provides simultaneous and collocated measurements of wind and waves, which is very important to offer a better validation of wave models and progress in the analysis of wave physics and air–sea interaction processes. Furthermore, the two instruments on-board CFOSAT (SWIM and a wind scatterometer called SCAT) are new technical concepts (with for both, a beam rotating scanning geometry) which have pushed the technology ahead.

In this context, the aim of this article is to discuss the first results obtained with the SWIM instrument from the verification phase. The results presented here summarize the results obtained by the Wind and Wave Experts groups organized by the CNES to validate the SWIM data.

This article is organized as follows. Section II recalls the main characteristics of the mission and the SWIM instrument. Section III summarizes the main content of the scientific products and explains the methods and tools used for the validation. Section IV provides a summary on the SWIM instrument performance. Section V shows the results on the nadir beam products (wave height, normalized radar cross section, and wind speed similar to other altimeter missions). Section VI discusses the results obtained on the normalized radar cross section in a diversity of observation geometry (diversity of near-nadir incidence and azimuth angles). Section VII presents the results of the fluctuation and speckle spectra which are intermediate quantities between the normalized radar cross section and the final Level 2 product (wave spectra). Section VIII presents an assessment of the wave spectral parameters. Finally, Section IX summarizes the results, indicates the work under progress to improve the processing and the products, and concludes.

II. MAIN CHARACTERISTICS OF THE MISSION AND THE SWIM INSTRUMENT

A. Mission

To meet the objectives recalled in Section I, the satellite carries two payloads; both are Ku-band radars scanning around the vertical axis:

- 1) The wave scatterometer SWIM operating at 13.575 GHz, a rotating six-beam radar at small incidence angles (0–10°) [2].
- 2) The wind scatterometer SCAT operating at 13.256 GHz, a fan-beam radar at larger incidence angles (26°–46°) [5].

CFOSAT was launched on October 29, 2018, on a low altitude sun-synchronous orbit (around 500 km). The main characteristics of the CFOSAT orbit are summarized in Table I.

The main objective of SWIM is to provide directional wave spectra as explained in [2]. The main products delivered to users are:

TABLE I
CFOSAT ORBIT CHARACTERISTICS

Orbit radius	6891.987 km
Altitude at the equator	514 km
Inclination	97.465°
Nodal period	94.761 min
Local time of descending node	7:00 AM +/- 30 min
Longitudinal step between two ascending nodes	23.756° (~2644 km)
Longitudinal step between two descending nodes	1.827° (~203.4 km)
Cycle duration	13 days
Number of sub-cycles	2
Number of orbits per cycle	197

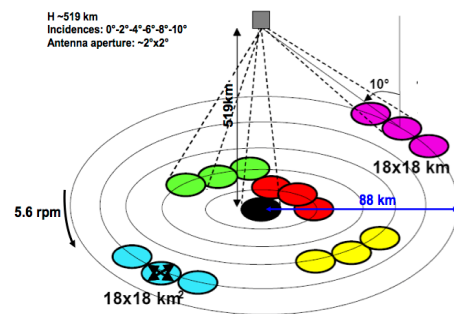


Fig. 1. SWIM beam rotation and incidence angles.

- 1) Significant wave height (H_s) and wind speed from the nadir measurements.
- 2) Directional wave spectra and their parameters from the off-nadir beams pointing at 6°, 8°, and 10° mean incidences.
- 3) Normalized radar cross section profiles from 0° to 10°.

B. Measurement Concept and the Main Characteristics of SWIM

The concept of SWIM is based on a scanning-beam real-aperture radar, following the ideas proposed in the 1980s by Jackson *et al.* [6], [7], both for airborne and spaceborne configurations. This concept has been implemented and validated on various airborne systems [8]–[11]) but SWIM is the first spaceborne instrument working with this concept. As recalled in [2], the main idea is that at near-nadir incidence (around 8°–10° from nadir), the normalized radar cross section is sensitive to the local slope of the sea surface but almost insensitive to small-scale roughness effects produced by the wind and to hydrodynamic modulations resulting from interactions between short and long waves. Hence, the main factor which modulates the normalized radar cross section is the tilt of the long waves when the radar looks in their direction of propagation. Details on the theoretical basis of the concept and wave spectra inversion in the configuration of SWIM can be found in [2].

In order to exploit this concept and provide complementary observations from the nadir and near-nadir measurements,

TABLE II
MAIN PARAMETERS OF A NOMINAL MACROCYCLE

Beam	0	2	4	6	8	10
Time duration (ms)	55.4	22.6	22.6	34.4	40.5	44.2
Number of integrated echoes	264	97	97	156	186	204
Number of averaged range bins	1	4	4	2	3	3

the design was chosen as recalled below. SWIM is a Ku-band radar with a multiincidence and scanning azimuthal geometry (Fig. 1). It illuminates the surface sequentially with six incidence angles: 0°, 2°, 4°, 6°, 8°, and 10°, each beam with a beam aperture in elevation and in azimuth of 1.5°–1.8° (see [2]). Given the orbit height, the footprint dimension of each beam is about 18 km × 18 km, and the full swath for the outer beam (10°) is about 90 km in radius. In order to acquire data in all azimuth directions, the antenna beam is rotated at a speed rate of 5.6 r/min, which generates, when combined with the satellite advection, some overlap in the sampling of successive rotations (see [2]). Off-nadir beams at 6°, 8°, and 10° are also called the “spectral beams,” as these beams are used for 2-D wave spectra estimation and wave spectra parameters.

The range detection is achieved by using a 320-MHz chirp for the 50- μ s pulses, providing a theoretical 0.47-m range resolution. All sequences of acquisition start with nadir sampling, which is used like on altimeter missions, to track the distance of the signal and adapt the receiving chain in consequence. The nominal sequence of acquisition follows the one given in Table II leading to a macrocycle duration of about 220 ms (a macrocycle is defined as the sequence of illumination performed between starting again the nadir tracking). During a nominal macrocycle, the azimuth rotates by about 7.5°. The on-board processing of the raw signal includes numerical range compression with a compensation for range migration during integration time (see [2]). Further steps in the on-board processing include incoherent time and range averaging over durations and number of samples which vary with the beam (see Table II).

C. Scientific Product Specification

As described in [2], the specification on the scientific products was defined during the mission development as given in Table III.

III. DATA SETS AND VALIDATION METHODS

A. Products From the French Mission Centers

From the raw data downloaded to the French Mission Center [CFOSAT Wind and Waves Instrument Center (CWWIC)], the following products are generated by the processing chain and made accessible to users:

- 1) *L1a*: normalized radar cross section σ_0 for beams 0–10° at the resolution and sampling of the raw downloaded data, with associated geolocalization.

TABLE III
PRODUCT SPECIFICATION

From nadir observations	Significant wave height better than 10% or 50 cm (maximum)
	wind speed with accuracy of approximately ± 2 m/s or 10% (whichever is greatest)
From off-nadir beams	Two-dimensional wave spectra at a scale of 70 km x 90 km, wavelengths detected from 70 m to 500 m
	Dominant wavelengths with an accuracy of 10%, for up to three wave partitions of the wave spectrum
	Dominant directions with an accuracy of 15°, for up to three wave partitions (keeping 180° ambiguity in direction)
From all beams	Significant wave height accuracy better than 10%, for up to three wave partitions
	σ_0 values as function of incidence and azimuth, every 0.5° in incidence and 15° in azimuth

- 2) *L1b*: intermediate products for the generation of wave spectra, only over ocean and for beams 6°, 8°, and 10°: relative fluctuations of σ_0 within each footprint, associated fluctuation spectra with and without speckle corrections.
- 3) *L2*:
 - a) From the nadir beam (0°) over the ocean: significant wave height, normalized radar cross section, and surface wind speed (tentatively mss) using a new retracking algorithm (see Section V).
 - b) From the nadir beam over ice and continent, the main parameters are the normalized radar cross section and parameters of the echo shape (width of the leading edge and slope of the trailing edge in three domains) (see [12]).
 - c) For beams at 6°, 8°, and 10°, over ocean only: 2-D wave spectra provided in 12 directions from 0° to 180° and 32 wave number bins unequally spaced from $k_0 = 0.0126$ to $k_{\max} = 0.2789$ rad/m (with width Δk of each wavenumber bins following $\Delta k/k = 10\%$); each 2-D spectrum is constructed from observations of successive overlapping antenna scans over 180° (on each side of the track) and representative of wave cells (boxes) of about 70 × 90 km².
 - d) The main parameters (wave height, dominant direction, and wavelength) of the wave spectra and of up to three wave partitions.

B. Validation Tools and Methods

It should first be noted that only data posterior to April 25, 2019, have been used, because prior to this date, an error was remaining in the on-board processing (in the migration compensation algorithm) which induced an important filtering of the detected waves. Most of the validation has been done by gathering SWIM data sets acquired all over the global ocean (excluding, however, sea-ice-covered regions).

TABLE IV
SWIM FUNCTIONAL AND PERFORMANCE VALIDATION

Power consumption	189W, stable in time
Temperature	Compliant with spec., stable
Coverage in tracking mode	Compliant with spec., stable
Antenna rotation speed	Compliant with spec., stable
Estimated pointing accuracy	$< 0.1^\circ$
Point Target Response	Maximum power variation < 0.2 dB
	Range drift (6 months) : 52.60 mm
	3 dB resolution : 2.7875ns ± 0.1 ns
	Side lobe dissymetry (1 st to 5 th) < 1 dB Integrated 1 st side lobe ratio 10.10 dB ± 0.05 dB
Instrumental gain	Compliant with spec., stable
Antenna gain w.r.t. azimuth	Differences w.r.t. on-ground estimation < 0.5 dB

This is why we mainly rely in this article on numerical model outputs as reference to analyze the Level 2 SWIM data on a statistical point of view, in particular the wave spectra and their parameters. Section VIII, however, presents the first comparisons with *in situ* observations.

For the nadir wind and wave products, the reference is mainly the European Centre WAVE Model (ECWAM) wave model from the European Centre for Medium-Range Weather Forecasts (ECMWF) and products from altimetry (Jason-3 and AltiKa). For off-nadir wave spectral data, the reference comes from the Meteo-France Wave Model (MFWAM) wave model. This latter is a third-generation model based on the ECMWF version (ECWAM-IFS-38R2) but with a slightly modified parameterization taken from the Wave Watch 3 (WW3) model [13, 14]. The MFWAM wave products used here have a grid size of 10 km and are driven by 3-h analyzed winds from the IFS-ECMWF atmospheric system. The model MFWAM accounts wave/current interactions with daily surface currents provided by the global PSY4-CMEMS ocean forecasting system. The wave spectrum is discretized in 24 directions and 30 frequencies starting from 0.035 to 0.58 Hz (1300–5 m of wavelength). The operational model MFWAM uses the assimilation of Hs from altimeters and directional wave spectra from Sentinel 1A and 1B. The MFWAM postprocessor includes a partitioning method to split the spectrum into wind sea and primary and secondary swells (see Section VIII).

For near-nadir normalized radar cross sections, we used statistics of the Global Precipitation Mission (GPM) data as reference values [15].

IV. SWIM INSTRUMENTAL PERFORMANCE

During the first month after launch, internal and antenna calibration sequences were performed continuously over several days. The analysis of the instrumental parameters such as the point target response (PTR), the radar gain, and the antenna rotation speed shows that all are comparable with the ground measurement values, very stable in time, and well within the requirements (see Table IV).

The instrument performance is primarily evaluated via its PTR. A performant measurement of this parameter means a good precision of the radar measurement. After range

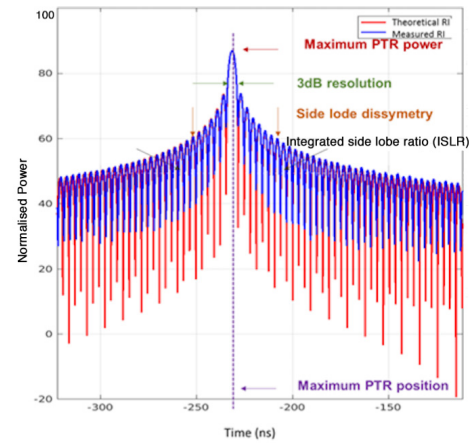


Fig. 2. PTR. Blue line: the measured PTR and red line: the theoretical sinus cardinal function.

compression, the PTR of a punctual target is expected to be a cardinal sinusoidal function with resolution at 3 dB inversely proportional to the signal bandwidth. This bandwidth defines the range resolution of the received signal. The internal calibration is used to evaluate the PTR function performance and, thus, the possible internal drifts related to the instrument through the derived PTR parameters. As shown in Fig. 2, the in-flight measured PTR (in blue) matches very well the theoretical impulse response (in red). One can see some differences between these curves, but they are all located at the low-energy minima of the sinc-shaped PTR. The total integrated power from the measurements fits the theoretical value within 95%. The fit between the measured and theoretical PTRs is higher than 98% if the integrated power is estimated over the principal lobe and the five first sidelobes. Note that these latter parameters are part of the monitored PTR parameters used to assess the instrumental performance on a regular basis.

SWIM instrumental parameters are monitored daily with routine calibration sequences performed since December 2018 (three internal calibrations and one antenna calibration sequences per day). The performance of these parameters, from the launch to the end of commissioning phase, is synthesized in Table IV. This allows a reliable absolute calibration of SWIM σ_0 , when correcting the acquired power from all instrumental contributions.

We can first highlight the good instrumental behavior of SWIM by its tracking mode from the nadir beam. Table V compares the tracking rate for the SWIM instrument and the ongoing altimeter Poseidon-3B on-board Jason-3, which uses a median tracker, similar to SWIM. The comparison is shown over one cycle (13 days and 10 days, respectively), both over open ocean and globally. First, SWIM tracking mode shows similar performances to conventional altimetry over ocean, with a 99.96% and 99.98% coverage during one cycle, respectively. The higher tracking performances of the SWIM instrument are then highlighted over land, ice, and sea ice. Thanks to the improved on-board signal processing, the tracking rate for SWIM is raised by more than two points regarding Poseidon-3B particularly over ice and land and reaches 98.48% over 13 days.

TABLE V
TRACKING RATE FOR THE SWIM NADIR BEAM AND POSEIDON-3B
ON-BOARD JASON-3 (STATISTICS OVER 13 DAYS FOR
SWIM AND 10 DAYS FOR JASON-3)

	Over ocean	Over all surfaces
SWIM	99.96%	98.48%
Poseidon-3B	99.98%	96.26%

TABLE VI
AVERAGED SNR

Beam	6°	8°	10°
Mean mid-swath SNR	>15 dB	~15 dB	~10 dB

Second, the signal-to-noise ratio (SNR) was analyzed for each beam. Table VI gives the averaged values of SNR, computed from the midswath radar gates over one cycle for the 6°, 8°, and 10° beams. SNR shows the contribution of instrumental noise (mainly thermal noise) with respect to the total measured signal. The higher the SNR is, the more accurate are the measurements and the instrumental noise is negligible in the total measured power. In the case of the SWIM instrument, midswath SNR values are 5–7 dB higher than expected worst cases, which confirms the good performance of the measurements and their high sensitivity to the ocean surface. This parameter is used to select the reliable swath of each of the spectral beams before the inversion of the 2-D wave spectra.

To compute the SNR, thermal noise floor is estimated for each macrocycle and each beam. It is first estimated from the 2° beam echo which exhibits in all conditions a very constant noise floor in the first range gates (at distances less than the altitude). The noise floor is estimated over the 60 first range gates. As the reception window width for the other beams does not allow the detection of a noise floor, the 2° noise floor is then propagated to the other beams.

Third, SWIM pitch and roll mispointing angles are also monitored and estimated through the Level 1A processing. The algorithm is based on the minimization of a cost function which computes the distance between the measured and a model echo power for a given measurement (at a given beam, antenna azimuth angle and elevation range). Both are corrected for geometric considerations, thermal noise, and instrumental contributions but not for the antenna gain. By minimizing the distance between measurement and model, we retrieve the mispointing angles in both the roll and pitch directions. Mispointing estimations obtained from this method (named method 1 hereafter) were compared to those obtained from two other methods: analysis of the difference between the theoretical and measured roll and pitch angles of the platform (method 2) and analysis of cross-maneuvers performed during 2 days in pitch and roll directions (method 3). Absolute mispointing angles estimated through these different methods are all of the order of 0.02°, i.e., one order of magnitude better than specified in the original requirements (0.2°). The angles derived from methods 1 and 2 are consistent: they show the same mean absolute mispointing angles of 0.02° (averaged over one cycle of data) and similar temporal variations.

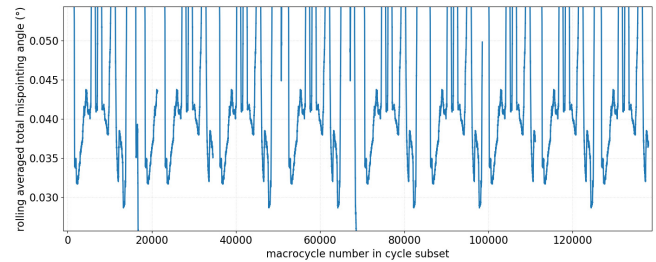


Fig. 3. Rolling average of the total mispointing angles estimated in the Level 1A processing over several orbits of 1.5 h each, with respect to macrocycle number in the selected subset. Values are averaged over 500 macrocycles. The oscillations show the impact of the reference ellipsoid.

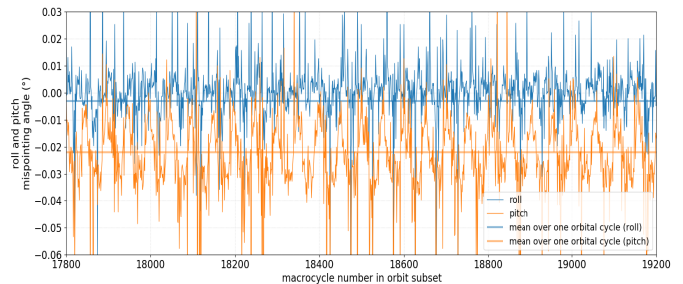


Fig. 4. Zoom of roll (blue curve) and pitch (orange curve) mispointing angles estimated in the Level 1A processing over about 5 min. The thick blue and orange horizontal lines show the mean roll and pitch angles, respectively, averaged over one cycle of data (13 days).

Fig. 3 shows for method 1 the total mispointing angle (defined as $(\text{roll}^2 + \text{pitch}^2)^{0.5}$) over several orbits). It highlights the impact of the reference ellipsoid, with oscillations of the total mispointing at the scale of the orbit (1.5 h). Fig. 4 illustrates the variation over a few minutes of both roll (blue curve) and pitch (orange curve) mispointing angles. Oscillations visible on both angles show the impact of the antenna rotation. The results from method 2 give similar variations (not shown). As for the results from the cross-maneuver method (method 3), they confirm the order of magnitude of the retrieved mispointing values but cannot be used to follow variations with the antenna rotation or along the orbit, as they provide only occasional estimates of roll and pitch mispointing angles. Thus, in practice, Level 1A estimation is used for monitoring and stability assessment of SWIM mispointing. It is also used as input of the nadir beam echo inversion (see Section V) and the antenna gain pattern for the off-nadir beams (see Section VI).

V. NADIR BEAM PARAMETERS

In a way similar to standard satellite altimeter missions, geophysical parameters from the nadir echo waveform over the ocean are inverted by applying a “retracking” algorithm based on the fit of a Brown model echo [16] to the recorded waveforms. For SWIM, however, no information is provided on the epoch or height because CFOSAT is not an altimeter mission (no precise orbit determination, no microwave radiometry, or no dual-wavelength measurement for delay correction).

Over ocean surfaces, the main geophysical products are, thus, the significant wave height, the normalized radar-cross

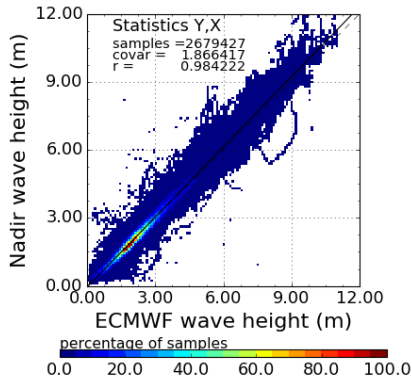


Fig. 5. Significant wave height from the SWIM nadir observations compared to ECMWF model data for a 13-day period (September 9–21, 2019).

section σ_0 , and the wind speed. An innovative algorithm, namely “Adaptive retracking” [17] is implemented in the CFOSAT French ground segment. This “adaptive” algorithm has three specificities with respect to algorithms currently used for most of other altimeter missions.

- 1) It considers the real PTR (estimated from on-board calibration sequences) instead of a theoretical function.
- 2) The Brown model is determined taking mispointing values issued from Level 1A processing as inputs. This gives access to the mss of the waves.
- 3) The minimization is carried out according to a maximum likelihood criterion with the Nelder–Mead inversion method [18].

The retracking is performed at the rate of the nadir echo acquisition (every 220 ms in the nominal mode of SWIM acquisition), and the geophysical products are provided either as “native” values (at 4.5 Hz) or as averaged values (1 s, 4.5 s, or per box). This Adaptive retracking method shows the remarkable results for all the retrieved parameters as detailed below.

A. Significant Wave Height

We have compared the significant wave height from the SWIM nadir observation to collocated model data (ECMWF WAM and MFWAM). The result shows a very weak and stable bias: about 3 cm with respect to ECMWF over a one orbital cycle period (see Figs. 5 and 6), and 1 cm with respect to MFWAM, over 3 months. As shown in Fig. 6, this bias is only slightly variable with wave height, and the dependency with wind is almost negligible. Fig. 7 shows the comparison with Jason-3 data. It also highlights a very small bias, with a mean difference less than 1 cm and a standard deviation of 35 cm. The same kind of results was obtained for comparison to AltiKa data, with a mean Hs difference of 6 cm with respect to AltiKa and a standard deviation of 35 cm.

B. Normalized Radar Cross Section

The nadir normalized radar cross sections from SWIM were compared to those provided at crossover points by the altimetry missions Jason-3 and AltiKa. Fig. 8 highlights a remarkable consistency with the Jason-3 data with a mean

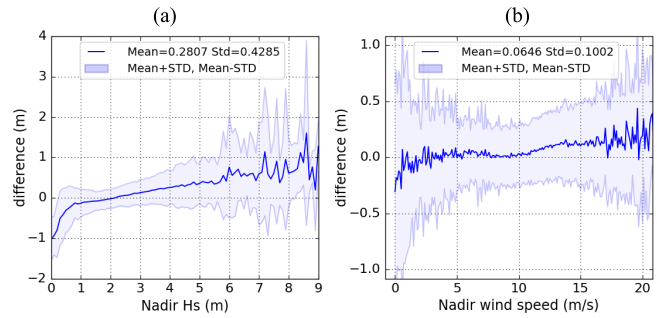


Fig. 6. Difference between SWIM and ECMWF significant wave height. (a) As a function of significant wave height. (b) As a function of wind speed. Blue/light blue: mean/one standard deviation envelope.

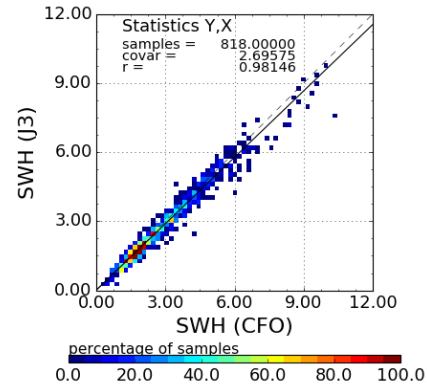


Fig. 7. Significant wave height from the SWIM nadir observations compared to Jason-3 altimeter values at crossover points for time difference less than 3 h (1 orbital cycle: August 14–26, 2019).

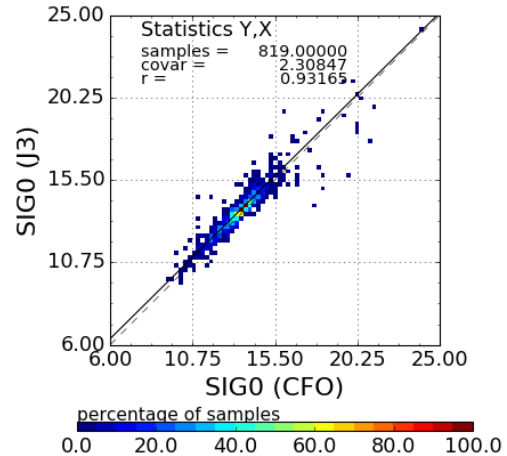


Fig. 8. Same as Fig. 7 but for the nadir σ_0 values.

difference of about 0.25 dB with respect to Jason-3 (standard deviation 0.6 dB); the mean difference with the AltiKa Ka-band instrument is around -2.5 dB (standard deviation 0.7 dB) with latitude dependency, as expected due to the different operation frequency (Ku-band versus Ka-band).

C. Wind Speed

Nadir wind speeds provided in SWIM products are computed with the algorithm [19] used operationally for the

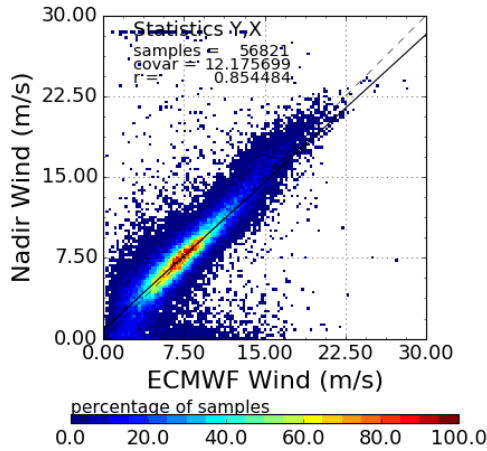


Fig. 9. SWIM nadir wind speed compared to ECMWF wind speed for a 13-day period (September 9–21, 2019).

Jason altimetry missions. These estimations are compared with the ECMWF model data in Fig. 9.

The mission accuracy specification of less than 2 m/s for wind speed is globally satisfied. However, the nadir sensor tends to overestimate low winds (below 8 m/s) and underestimate higher winds when one takes the model estimations as reference data. A study is underway to reduce such discrepancies by developing an adapted algorithm based on the nadir data themselves to better reflect their behavior. The algorithm will take the form of a 2-D Lookup table depending on the data pair (σ_0 , H_s) as proposed in [20]. One year of data will be analyzed to ensure that a stable statistical model will be obtained and that all seasonal conditions have been observed between roughness, and wind and wave parameters.

In the nadir product, a rain flag is defined following the principle proposed in [21] and used for AltiKa data. This method was adapted to SWIM during the first months of the mission. The first results indicate a good consistency between the flags raised and rain provided by collocated radiometers (see [17]). The flag is also used to flag “bloom” events but some tuning is still necessary for this part.

One of the motivations for choosing the “Adaptive” retracking method was to reduce the impact of the relatively low nadir measurement rate of SWIM (at 4.5 Hz approximately due to time spent on illuminating the off-nadir beams). An analysis was performed to qualify and quantify the improvement of adaptive retracking with respect to the conventional altimetry retracking algorithm based on the maximum likelihood estimator MLE4. By using a spectral analysis of significant wave height series along-track, we found a 45% reduction of noise which allows to get the same performance in the SWIM nadir product (20-cm rms noise) for 4.5-Hz measurement rate and in Jason-3 official product (20-Hz measurement rate). Significant improvements are also observed in the σ_0 restitution, as described in [17].

VI. NORMALIZED RADAR CROSS SECTION OF OFF-NADIR BEAMS

The normalized radar cross section σ_0 is provided for all the SWIM beams from 0° to 10° and for all scenes

(ocean, continent) as far as the nadir tracking has been successfully achieved with the on-board processing. At Level 1A, σ_0 is provided over the successive footprints (about 18 km in length) with a discretization of 1.4 m (for the antenna beams 2° and 4°), 0.7 m (for the antenna beam 6°), or 1 m (for the antenna beams 8° and 10°). As SWIM is a real aperture radar, σ_0 measurements refer to azimuthally integrated quantities (over about 18 km perpendicularly to the line of sight). At Level 2, σ_0 is provided as the averaged values per bins of 0.5° in incidence and 15° in azimuth, and referenced in the geometry of the wave cells, with one box every 70 km (approximately) on each side of the nadir track (see the next section for the geometry of the cells).

When converting the radar echo to σ_0 values, the classical radar equation is considered; it includes geometrical and radiometric corrections. For the geometrical corrections, the altitude of the satellite is provided by the epoch of the nadir beam of the same macrocycle. The mispointing angles estimated as explained in Section IV are used to apply an antenna gain pattern compensation (azimuthally integrated value) which is taken from precalculated look-up tables parameterized as a function of incidence, azimuth angles, and roll and pitch angles. Finally, at Level 1A, σ_0 values are corrected from the thermal noise by subtracting the mean value of the thermal noise estimated as explained in Section IV. For the radiometric corrections (instrument gain and losses), the calibration coefficients from the most recent on-board calibration sequence is taken into account and the thermal noise mean level is subtracted. Note that no atmospheric correction is applied at Level 1A. In contrast, Level 2 includes such a correction to account for attenuation by the dry atmosphere and wet atmosphere (water vapor and liquid cloud water taken in auxiliary files generated from ECMWF model short-term forecasts).

Fig. 10(a) illustrates the mean trend of σ_0 obtained from L2 products from the different beams (values averaged every 0.5° in incidence and 15° in azimuth). The mean trend is globally consistent with the results provided by GPM data sets [15] [see Fig. 10(b)]. The relative biases of σ_0 between the different SWIM beams are very small (of the order of 0.1–0.2 dB according to Fig. 10(a) except between beams 2° and 4°). A detailed analysis is in progress to estimate more precisely the possible biases between the different SWIM beams.

Fig. 11 illustrates the dependence of σ_0 with wind speed. The SWIM data are very consistent (less than 1-dB difference) with the GPM data mean trend. The sensitivity to wind speed is very small for the 10° and 8° beams (1–1.5-dB difference between 5 and 20 m/s) and gradually increases at smaller incidence angles. Thanks to this smallest sensitivity of σ_0 with wind speed at 8° and 10° , the dominant effect in the σ_0 fluctuations at the scale of the footprint will, hence, be the tilt of the long waves, so that the best results for the wave inversion are expected to come from these incidence ranges. At light winds (typically less than 4–5 m/s), we can observe some outliers with low σ_0 values in Fig. 11. Such outliers may come from nonstandard scenes (for example, affected by rain); note that it was chosen for the data analysis dedicated

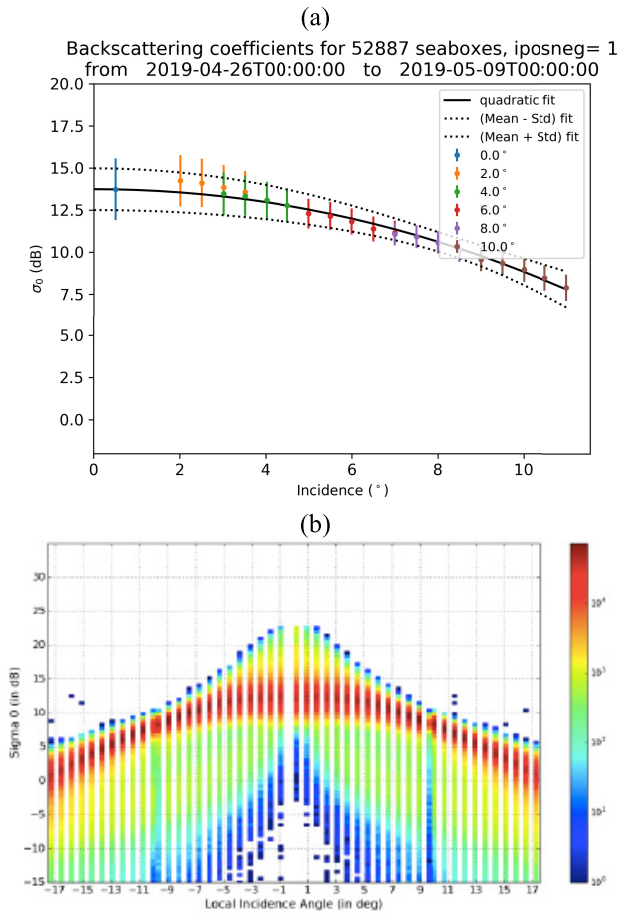


Fig. 10. (a) SWIM mean profiles of σ_0 with incidence angle over the free ocean surface. (b) Statistics of σ_0 from GPM/PR data for negative and positive incidence angles with respect to nadir (N. Longepe, personal communication).

to the validation, as presented here, to keep all data without rejections. Starting mid-2020, the operational processor will be configured with additional quality controls to account for either the nadir rain flag or a flag specific for off-nadir beams based on the mean and standard deviations of σ_0 .

VII. FLUCTUATION SPECTRA AND SPECKLE NOISE

A. Characterization of the Fluctuation Spectra

During the verification phase, one of the first steps was to assess the properties of the fluctuation density spectra. These spectra are defined as the Fourier transform of the autocorrelation function of the σ_0 fluctuations projected on ground within each footprint [2]. At first, the general behavior of these fluctuation spectra was evaluated by analyzing the mean spectra. These latter are obtained for each SWIM beam, by averaging fluctuation spectra over several days and all geographical positions. So it accounts for all kinds of sea-state conditions. These averaged spectra are used here to qualify the wavelength and the azimuth ranges which are adequately imaged by SWIM. The left part of Fig. 12 displays such a mean spectrum, for the 10° beam, based on an average over 6 days of observations on the ocean. On the right-hand side of Fig. 12, the corresponding mean wave slope

spectrum calculated from collocated WW3 model wave spectra is shown (averaged over the same positions and dates). First, Fig. 12 shows that outside an angular sector of $\pm 15^\circ$ with respect to the satellite track, the characteristics of the mean fluctuation spectrum are similar to those of the mean WW3 slope spectrum, with the most energetic parts spanning over wavelengths from 125 to 450 m and direction around the 45° in the mean. It also shows that within an angular sector of about $\pm 15^\circ$ on each side of the along-track direction, there is a strong increase in the energy level not related to the surface ocean waves. Very similar results were obtained for the 6° and 8° beams. The energy peak in the along-track direction is due to an increased noise in the directions where the Doppler bandwidth becomes relatively small (due to the geometry of observations). This causes a drastic drop in the number of independent samples [22] which increases the speckle noise.

This effect was anticipated before the satellite launch but its exact magnitude could not be simulated precisely. Fig. 13 illustrates for all beams (from 2° to 10°), in a polar representation, the correlation coefficient between the SWIM fluctuation spectra and the corresponding WW3 wave slope spectra, over the same time period as in Fig. 12. It shows that for beams 6° , 8° , and 10° , the correlation coefficient is larger than 0.5 for all wavelengths greater than about 60 m and in all directions, except in the along-track sector affected by the increase of speckle noise. For beams 2° and 4° , the correlation with WW3 is degraded compared to the other SWIM beams (6° , 8° , and 10°). This was expected for the following reasons: 1) no migration compensation is applied in the on-board processing for the signals coming from these beams and 2) the range resolution is less than for the other beams (see Table II). Actually, these SWIM beams were not originally designed to retrieve ocean wave parameters, but they were mainly designed to provide the mean radar cross sections. Furthermore, at these near-nadir incidences, the relation between signal modulation spectra and wave slope spectra may become nonlinear due to range-bunching effects on the signal [23]. Nevertheless, Fig. 13 indicates that observations from these 2° and 4° SWIM beams contain information on waves while being more filtered than for the 6° , 8° , and 10° SWIM beams.

B. Density Spectrum of Speckle Noise

As explained in [2], [6], and [7], the speckle noise must be taken into account in the inversion process. In the spectral domain, the spectral density of speckle must be subtracted from the fluctuation spectrum in order to obtain a spectrum related to the surface ocean waves (hereafter called modulation spectrum)

$$P_{\delta\sigma_0}(k) \approx \delta(k) + P_{\text{IR}}(k)P_m(k) + P_{\text{sp}}(k) \quad (1)$$

where $P_{\delta\sigma_0}$ is the density spectrum of the signal fluctuations, P_{sp} is the density spectrum of the signal fluctuations due to speckle, $P_m(k)$ the density spectrum of signal modulations due to ocean waves, P_{IR} is the density spectrum of the impulse response, and δ is the Dirac function.

Assuming that the impulse response function follows a cardinal sine function in the temporal domain,

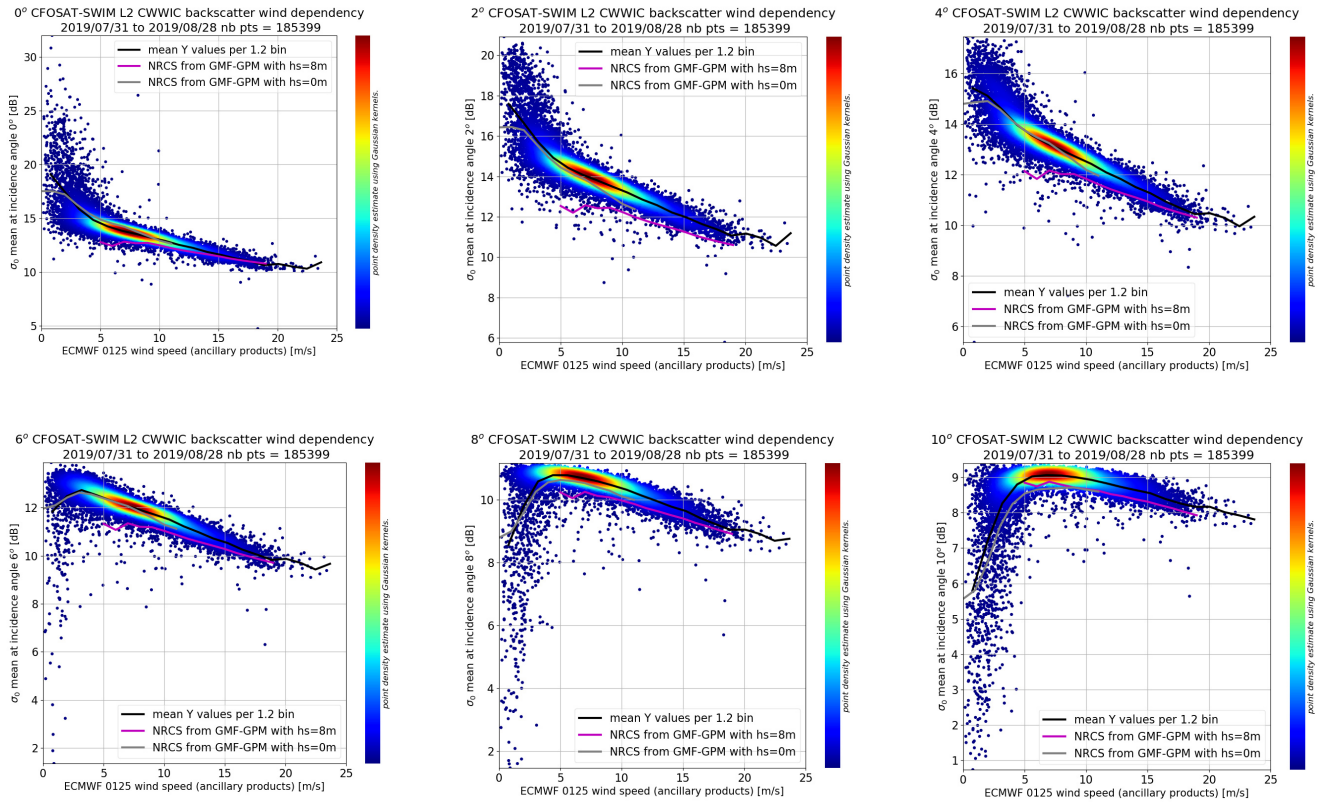


Fig. 11. Distribution of σ_0 values at 0° , 2° , 4° , 6° , 8° , and 10° ($\pm 0.5^\circ$) as a function of wind speed (taken from the ECMWF model). The black line shows the mean value. The color lines correspond to the mean values of GPM data for the same wind and significant wave heights of 0 (green) and 8 m (purple).

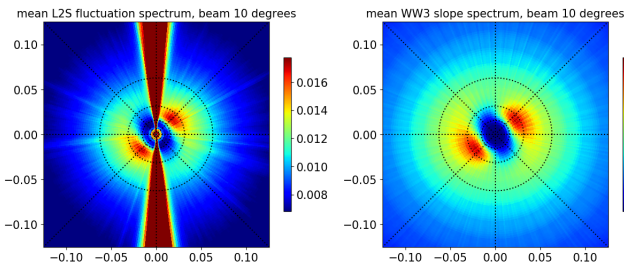


Fig. 12. (Left) Mean fluctuation spectra for the period from April 25, 2019, to April 30, 2019, compared to the (Right) mean wave slope spectrum obtained from collocated points of WW3 outputs. Horizontal and vertical axes refer to the wavenumber of the waves in two orthogonal directions, with the vertical axis aligned with the satellite along-track direction.

both $P_{IR}(k)$ and $P_{sp}(k)$ follow a triangle shape, and $P_{sp}(k)$ is given by the following equation:

$$P_{sp}(k) = \frac{1}{N_{ind}} \frac{\delta r}{2\pi} \frac{1}{\sin\theta} \text{tri}\left(\frac{k}{2\pi} \frac{\delta r}{\sin\theta}\right) \quad (2)$$

where tri is the triangle function, k is the wavenumber, δr is the radar range resolution, θ the incidence angle, and N_{ind} is the number of independent samples.

Equation (2) is different from (13)–(15) in [2] because it now takes into account the real shape of the impulse response function. It follows a cardinal sine shape instead of a Gaussian shape as assumed in [2]. In the default option of the operational processor (used until mid-2020), the number of independent samples N_{ind} was assumed to be the number

of echoes integrated in real time (Table II), so that the speckle energy correction was isotropic. However, it is clear from the analysis shown in Section VII-A (Fig. 12) that this latter assumption is not appropriate. Indeed, successive echoes are uncorrelated only if the Doppler bandwidth is much larger than the pulse repetition frequency (PRF) (see [22]). When looking along-track, this assumption breaks down, whereas other effects, which partially decorrelate successive echoes, may play a role. In the initial version of the processing, the speckle was also estimated assuming the intrinsic radar resolution (0.47 m), without taking into account a possible reduction of speckle level brought by consecutive range bins' averaging. Here, we present and use an empirical approach to estimate from the data themselves, the density spectra of the noise, on the one-hand outside, and on the other-hand inside the sector perturbed by the lack of radar Doppler bandwidth. Outside this sector, we hereafter call the analyzed spectra, the “background density spectrum of speckle.”

1) *Background Density Spectrum of Speckle*: Outside the sector impacted by the radar Doppler bandwidth reduction, we selected all fluctuation spectra from observations in directions which are the least affected by the ocean waves. They correspond to the direction of minimum fluctuation variances over each 180° azimuthal sectors swept by the beam rotation. The mean speckle noise density spectrum was then calculated by averaging this result over a large number of spectrum samples in different sea-state conditions. The mean speckle noise density spectra were, hence, estimated with the same

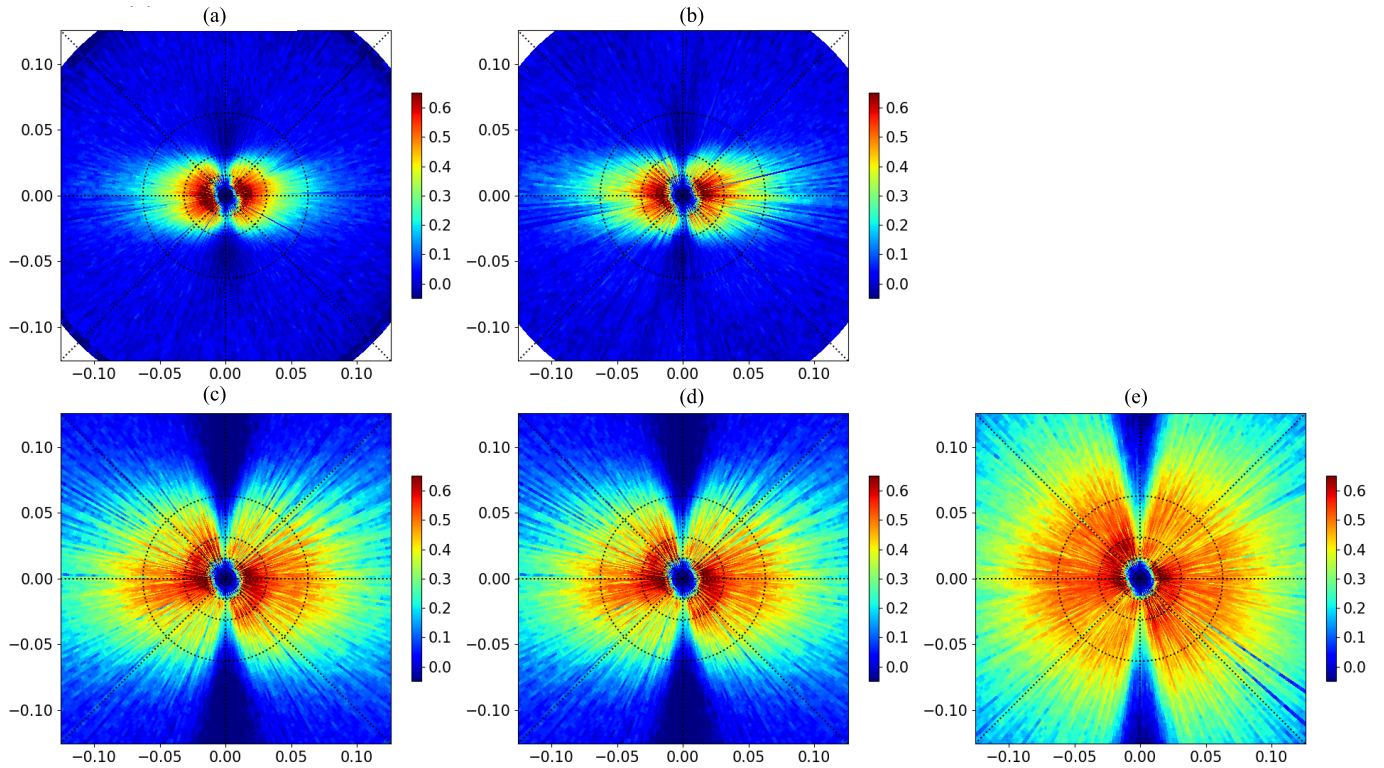


Fig. 13. Polar plots of the correlation coefficient between SWIM fluctuation spectra and WW3 collocated wave slope spectra for the data set from April 25 2019, to April 30, 2019. Horizontal and vertical axes refer to the wavenumber of the waves in two orthogonal directions, with the vertical axis aligned with the satellite along-track direction. (a)–(e) For SWIM beams 2° , 4° , 6° , 8° , and 10° , respectively.

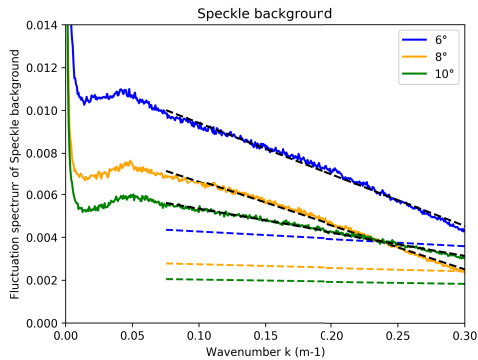


Fig. 14. Mean background density spectra as a function of wavenumber (rad/m) for beams 6° (blue solid), 8° (orange solid), and 10° (green solid). Black dashed lines correspond to the triangle-shaped model fit on these spectra (adjustment between $k = 0.075$ and $0.3 \text{ rad}\cdot\text{m}^{-1}$). Dashed colored lines correspond to (2) with the theoretical values of N_{ind} and δr . This figure corresponds to data selected over a 7-day period (April 26, 2019, to May 1, 2019) in the $[-10^\circ, 10^\circ]$ latitude range and for surface conditions with H_s less than 2 m and wind speed less than 5 m/s.

regular δk sampling as for the fluctuation spectra. In order to investigate the possible variation of this mean speckle spectral level with surface conditions or latitude, different classes of latitude and sea state were considered (classes identical to those used in Section VII-B2). The results indicate that the mean background speckle noise density spectrum does not depend significantly on sea-state conditions nor latitudes. This confirms that the background speckle is mainly dependent on the radar parameters and not on the surface conditions. Fig. 14 illustrates the results for one case, but the results

are very similar for the other conditions. Fig. 14 shows that the dependence of the speckle density with wavenumber k is almost linear in the range of $k = 0.05\text{--}0.3 \text{ rad/m}$, i.e., consistent with the linear model of (2). It also indicates that compared to the theoretical spectra obtained from (2) with theoretical values of N_{ind} (Table II) and with $\delta r = 0.47 \text{ m}$ (dashed lines in color), the speckle level estimated empirically is higher, at least for $k < 0.25 \text{ rad/m}$. When fitting (2) on the empirical spectra with N_{ind} and δr as free parameters (fit over wavenumbers in the $[0.075\text{--}0.30 \text{ rad/m}]$ range), we find larger N_{ind} and δr values compared to the theoretical values. This leads to values of the density spectrum at the origin ($k = 0$) which are 2.5 (2.2 and 1.9, respectively) larger than those corresponding to the theoretical values of δr and N_{ind} for beam 6° (8° and 10° , respectively). This ratio is close to the number of range gates averaged during the on-board processing (see Table II), which was not taken into account in the theoretical speckle estimates although it contributes to diminish the speckle spectral level. Note also that the larger δr values estimated from our empirical approach yield a faster decrease with wavenumber of the speckle level compared to the theoretical case (see Fig. 14). Combined with the different value at the origin, the two estimates of speckle level (theoretical and empirical) converge at large wavenumbers, around $0.2\text{--}0.3 \text{ rad/m}$.

2) *Density Spectrum of Noise Close to the Along-Track Direction*: In order to build an empirical model for the noise density spectrum close to the along-track direction, the approach was to analyze the fluctuation spectra as a function of wavenumber over a sector of $\pm 30^\circ$ from the

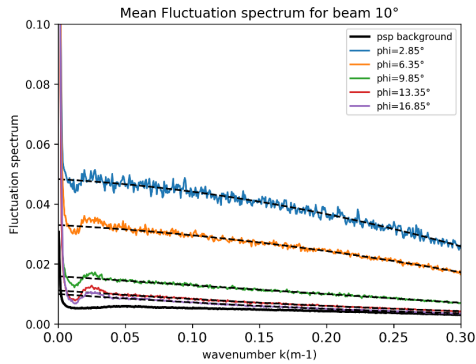


Fig. 15. Color lines: mean fluctuation spectra for the SWIM beam 10° obtained by accumulating data over different azimuthal angles (from about 2° to about 17° , with respect to the along-track direction, see insert legend) and over 6 days of observations (April 26, 2019, to May 1, 2019). The black dashed lines represent the polynomial fit (estimated for k within $[0.075\text{--}0.3]$ rad/m). The black solid line is the mean background speckle spectrum. See text for details.

along-track direction and its dependence on geometry of observation (latitude, look direction, and orbit orientation) and sea state. Twenty-one classes of data were selected for each SWIM incidence conditions (6° , 8° , 10°), composed of seven classes of latitude ($[-70^\circ, -50^\circ]$, $[-50^\circ, -30^\circ]$, $[-30^\circ, -10^\circ]$, $[-10^\circ, 10^\circ]$, $[10^\circ, 30^\circ]$, $[30^\circ, 50^\circ]$, and $[50^\circ, 70^\circ]$) and three classes of combination of wind speed U and significant wave height ($U < 5$ m/s and $H_s < 2$ m; $5 < U < 9$ m/s and $H_s < 2$ m; and $U > 9$ m/s and $2 < H_s < 4$ m). We choose the sea-surface classes so as to minimize the contributions of waves in the analyzed fluctuation spectra, while keeping enough samples to ensure a high statistical significance.

Fig. 15 shows the resulting mean spectra as a function of wavenumber (with the same wavenumber sampling as the fluctuation spectra) for the 10° SWIM beam and for one of these classes ($[-10^\circ\text{--}10^\circ]$ in latitude and $U < 5$ m/s). Solid lines with different colors are plotted for different directions of observation with respect to the satellite track. The results indicate that for azimuth angles from 0° to about 15° with respect to the satellite track, the shape and level of the spectrum change considerably, with energy significantly decreasing from 0° to 15° at all wave numbers. It stabilizes for azimuth angles larger than 15° (see the purple curve in Fig. 15). At these azimuth values, its level and shape become very similar to the background mean speckle spectrum, determined away from the along-track direction, as described in Section VII-B1, and identified by the black solid line in Fig. 15. Fig. 15 also illustrates that the increase of energy with respect to the background level is larger at small wave numbers, in the sector affected by the loss of Doppler bandwidth. These trends are similar for the other SWIM beams. However, the increase of the along-track fluctuation spectra with respect to the background speckle is much higher for the 6° beam than for the 8° and 10° beams. The trends with latitude and surface conditions are discussed later on in this section.

Our analysis led us to model the density spectrum of noise in this sector affected by the Doppler bandwidth reduction, as the

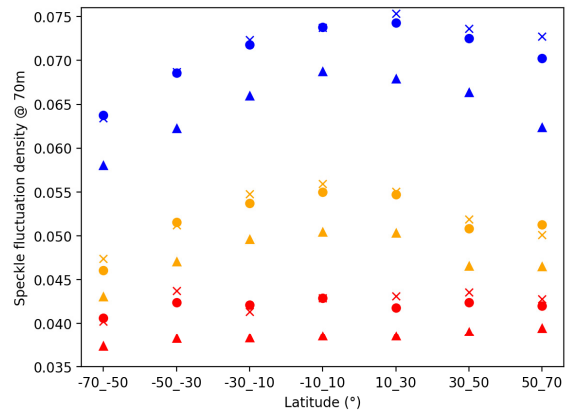


Fig. 16. Speckle noise spectral level at $k = 0.09$ rad/m (wavelength of ~ 70 m), calculated from our empirical formulation, at the azimuth angle of maximum speckle level ($\phi = \phi_0$). The results are plotted for the three SWIM beams in blue (6°), orange (8°), and red (10°) and three sea surface conditions (circle: $H_s < 2$ m and $U < 5$ m/s, cross: $H_s < 2$ m and $5 < U < 9$ m/s, and triangle: $2 < H_s < 4$ m and $5 < U < 9$ m/s).

sum of a second-order polynomial ($P_{sp}(k) = ak^2 + bk + c$) (to represent the trend with k as shown in Fig. 15) and a triangle function to account for the background noise discussed in Section VII-B1. Each coefficient of the second-order polynomial was then assumed to vary linearly with the azimuth angle:

$$a = a_0(\phi - \phi_0) + a_1, \quad b = b_0(\phi - \phi_0) + b_1, \quad c = c_0(\phi - \phi_0) + c_1 \quad (3)$$

where ϕ_0 is the azimuth angle at which $P_{sp}(k)$ was observed to be maximum.

We estimated ϕ_0 for different geometrical conditions, by analyzing the fluctuation spectra level $P_{sp}(k)$ at $k = 2\pi/30$ rad/m, in order to minimize the impact of long waves. It was found that ϕ_0 depends on: 1) latitude, with ϕ_0 almost aligned with the along-track direction at high latitudes and shifted to about $3.5^\circ\text{--}4^\circ$ from the along-track direction at latitude 0° ; 2) track orientation (changing sign between ascending or descending); and 3) look direction (uptrack or downtrack). All these dependencies have been taken into account in our model. Note that they are consistent with the fact that the effective Doppler bandwidth is impacted by these geometrical parameters, due to Earth rotation.

The dependence of the noise spectral level with both latitude and sea-state conditions was analyzed, based on the 21 pre-cited classes of data composed of seven classes of latitude and three classes of surface conditions. Fig. 16 illustrates, for each SWIM beam and for the three different classes of surface conditions, the trend of the energy level estimated with our empirical model at $k = 0.1$ rad/m and $\phi = \phi_0$, with respect to latitude. The results for other wavenumbers show the same trends. Fig. 16 first illustrates that the spectral level in the direction of maximum of speckle energy decreases from the 6° beam to the 8° and 10° beams, as in the case of the background speckle noise (Fig. 14). It also shows that for the three beams (6° , 8° , and 10°), the impact of sea conditions is significant for high wind speed conditions ($U > 9$ m/s), with a decrease of spectral level of 10% with respect to low and medium

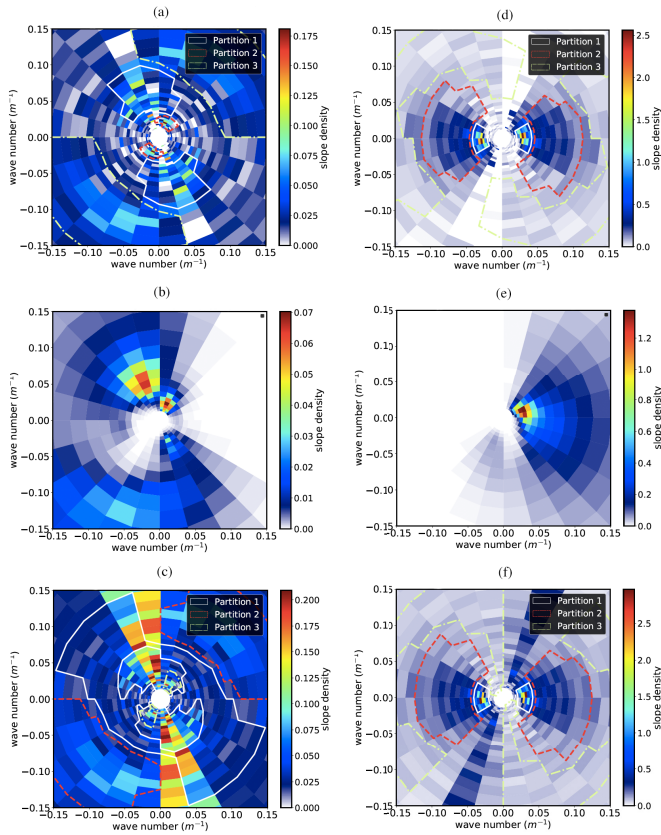


Fig. 17. Examples of wave spectra from the 10° beam observations with the speckle correction from the models presented in (a and d) this article and the (c and f) original correction. (b) and (e) Corresponding MFWAM wave slope spectra. The horizontal and vertical axes refer to East–West and North–South directions, respectively. The white, red, and yellow contours on the SWIM spectra indicate the partitions (see Section VIII). Date and position of observations are (a)–(c) April 26, 2019, 02:35 UTC at $[5.68^\circ \text{ N}, 113.27^\circ \text{ W}]$ and (d)–(f) April 26, 2019, 05:08 UTC at $[45.49^\circ \text{ S}, 22.51^\circ \text{ E}]$.

wind conditions ($U < 5$ m/s). Hence, it appears that in these conditions where decorrelation is not ensured by the radar acquisition conditions, wind speed starts to play a role on the decorrelation of echoes (hence, on the noise spectrum) for wind intensities larger than about 9 m/s. The decrease of the spectral level of noise with increasing values of wind speed is compatible with a correlation time of the surface scatters decreasing with wind speed [24]. Finally, Fig. 16 indicates also that the variation with latitude is significant for beams 6° and 8° .

3) *Impact of Speckle Noise Correction*: Based on the analysis presented in Sections VII-B1 and VII-B2, we applied the empirical speckle correction using: 1) a triangular-shaped model outside the along-track direction and 2) a combination of the triangular-shaped model and a quadratic-shaped model in the azimuthal sectors up to 15° around the along-track direction. Fig. 17(a) and (d) shows two examples of directional wave spectra obtained by using this noise correction. They are compared to the collocated MFWAM spectra [Fig. 17(b) and (e)] and to the wave spectra obtained when using the original speckle model as implemented in the operational processing until mid-2020 [Fig. 17(c)–(f)]. In the first example [Fig. 17(a)–(c)], illustrating complex mixed sea conditions

in the North Pacific [see Fig. 17(b)], the new correction allows to detect the dominant wave systems, including the one propagating in the along-track direction. With the initial processing, this latter wave system was completely hidden by the noise signature. Also, the background noise is decreased with respect to the case with the initial speckle correction.

In the second example [Fig. 17(a)–(c)], where the dominant waves propagate across-track, the impact of the new correction with respect to the initial one is less important. Nevertheless, it consistently decreases the background noise and suppresses the maximum of energy along track. It has to be recalled that in order to mitigate the problem of insufficient elimination of the speckle noise in the initial version of the SWIM data processing, a mask was applied in the along-track sectors on the wave spectrum. With this improved noise correction, the mask is not used anymore.

VIII. WAVE SPECTRA AND ASSOCIATED PARAMETERS

The Level 2 products are mainly the wave spectra and their parameters. They are estimated from the L1b data according to the following main steps.

- 1) The modulation spectra are estimated in each look direction by subtracting a speckle noise spectrum to the fluctuation spectra. In this article, the speckle correction is carried out according to the empirical model presented in Section VII, i.e., with the version implemented in the operational processing chain (version 5.0), from mid-2020.
- 2) The modulation spectra are resampled in wavenumber; for the results presented here, 32 wave numbers in the range $[0.0126\text{--}0.279]$ rad/m, corresponding to the wavelength domain $\sim [22\text{--}500]$ m.
- 3) The modulation spectra are transformed into wave slope spectra by applying a “modulation transfer function” (MTF) which uses an estimate of the mean falloff of σ^0 with incidence angle, in each azimuth direction (see [2]).
- 4) The different directions of the wave spectra are then combined to build the polar 2-D directional wave spectra at the scale of “wave box” of about $70 \text{ km} \times 90 \text{ km}$ (in the nominal mode of SWIM acquisition).
- 5) A partition scheme based on the watershed algorithm as in [25] is applied to detect up to three partitions.
- 6) Wave spectral parameters (significant wave height, dominant direction and dominant wavenumber) are calculated on the polar spectrum and on its partitions.

A. Global Analysis of Wave Spectra and Wave Parameters

A global analysis of the wave spectra quality was carried out by comparing at the global scale, wave spectra from SWIM and the MFWAM wave model. The MFWAM model was chosen because in the context of the CFOSAT CAL/VAL, the forecast wave spectra are collocated in near-real time by Météo-France on a systematic basis. Two kinds of analysis are presented hereafter:

- 1) Analysis of the full spectral content and parameters: correlation index between spectra and the main parameters of the full wave spectra.

TABLE VII
PERCENTAGE OF PAIRS OF SPECTRA WHICH EXHIBIT A CORRELATION INDEX HIGHER THAN 0.5

Pairs of spectra	% of cases with $R > 0.5$
SWIM 6/ SWIM 10	71
SWIM 6/ SWIM 8	70
SWIM 8 / SWIM 10	85
SWIM 6 / MFWAM	39
SWIM 8 / MFWAM	57
SWIM 10 / MFWAM	68

THE DATA SET IS FROM APRIL 26, 2019, TO MAY 9, 2019

2) Analysis of the main parameters associated with the partitions of the wave spectra.

The main parameters which are analyzed hereafter are the significant wave height H_s , the dominant wavelength, and the dominant direction. From SWIM, they are calculated by the operational processor on the 2-D polar wave slope spectra. For MFWAM, the wave parameters provided as output of the Météo-France operational processor are converted to take into account the conversion of peak period to peak wavelengths, assuming the deep water dispersion relationship. Note that for the spectral partitions, the MFWAM model provides the mean periods and mean directions, whereas the parameters estimated on the SWIM data are dominant wavenumbers and direction. This might explain some slight differences in the comparison below (Section VIII-A2).

1) *Analysis of the Full Spectra Content and Parameters:* Following [26], the first step was to calculate a 2-D correlation index either between pairs of spectra themselves or between spectra from each SWIM beam and the MFWAM spectra. The results are presented in Table VII. The correlation index between spectra from pairs of SWIM beams is better than 0.5 for at least 70% of the cases with the highest correlations between beams 8° and 10°. The results also indicate that the 6° beam behaves slightly differently from the other beams. When correlation indexes are compared to H_s values, it appears that for all SWIM pairs, the highest values of the correlation index are observed for H_s larger than about 2 m. As for the correlation index between spectra from the SWIM beam and MFWAM, Table VII indicates that the correlation index is better than 0.5 for 68% of the cases for the 10° beam (57% and 39% for the 8° and 6° beams, respectively). These numbers indicate that the spectra from beam 6° are significantly less comparable to the MFWAM spectra than those from beams 8° and 10°. The low correlation values (less than 0.5) between the 6° beam spectra and MFWAM spectra mainly occur in regions with small H_s values (typically less than the order of 1 m).

Fig. 18 illustrates the scatterplots of the SWIM beam 10° parameters versus the MFWAM parameters estimated on the full spectra. The first row of Table VIII gives the corresponding statistical scores. For the significant wave height, the correlation is very high (0.97) and the rms difference is quite small (0.26 m), but the mean trend is characterized by a slope of 0.82. This yields an overestimation of H_s at small values ($H_s < 3$ m) and underestimation at large values

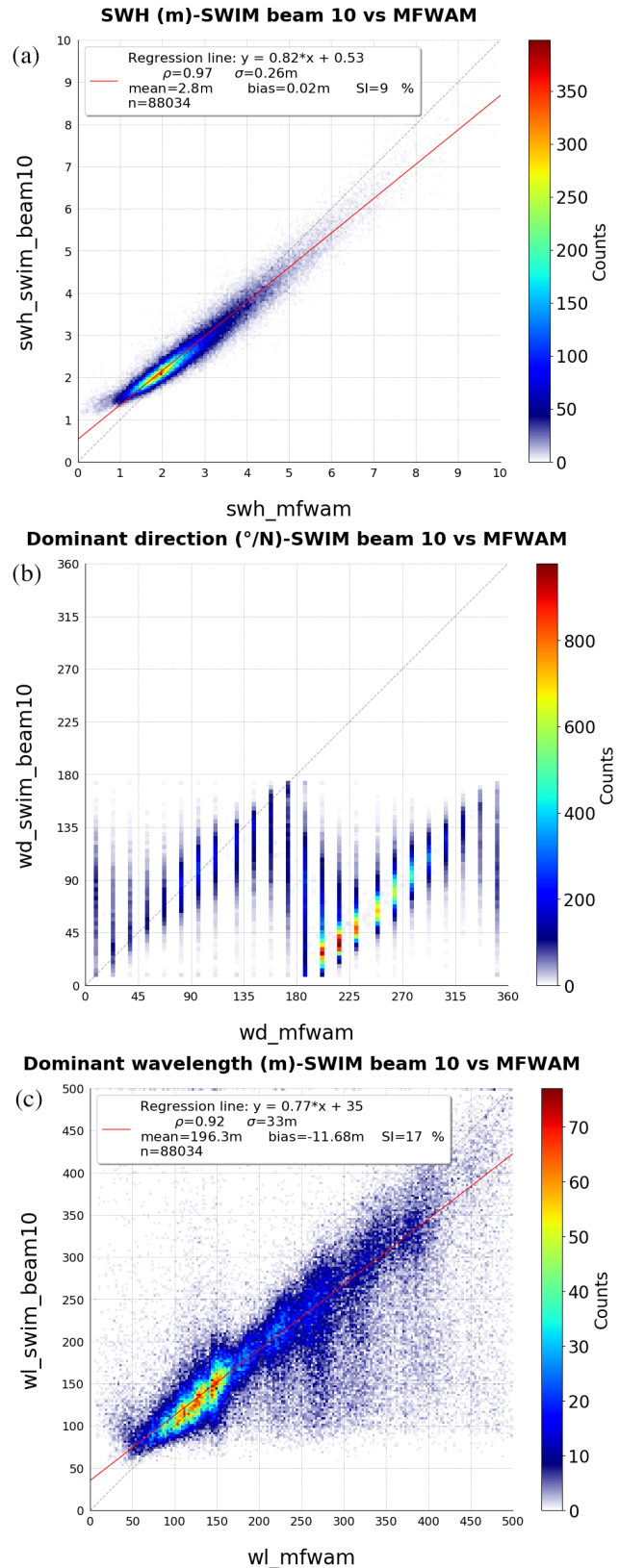


Fig. 18. Scatterplots of SWIM parameters from the 10° beam full spectra as a function of MFWAM full spectra parameters, for a 13-day period (April 26, 2019, to May 8, 2019). (a) Significant wave height H_s . (b) Dominant direction (from North). (c) Dominant wavelength. The color code represents the number of points per bin of values. The red line on (a) and (c) represents the linear fit.

TABLE VIII
STATISTICAL SCORES OF THE COMPARISONS OF WAVE HEIGHT,
DOMINANT WAVELENGTH, AND DOMINANT DIRECTION
FROM SWIM-BEAM 10° AND MFWAM

	Waveheight (m)	Wavelength (m)	Direction (°)
SWIM versus MFWAM- full spectra	0.82x+0.53 CC: 0.97 MB: 0.02m rms : 0.26 m SI: 9 %	0.78x +35 CC: 0.92 MB: -12.3 rms : 33 m SI 17%	0.59x+43 CC : 0.69 MB: 3.9° rms: 26°
SWIM 1 st partition versus MFWAM 1 st swell	0.73x +0.40 CC: 0.88 MB: -0.12 m rms : 0.40 m SI: 22%	0.83 x + 32 CC: 0.86 MB: 0.5 m rms : 45 m SI: 24%	0.57x+35 CC : 0.72 MB: 1.0° rms: 27°
SWIM partition matched to MFWAM 1 st swell partition	0.78x+0.18 CC: 0.89 MB: -0.22 m rms : 0.38 m SI: 23%	0.85x+35 CC: 0.90 MB: 5.6 m rms : 38 m SI: 19%	0.97x +6 CC: 0.98 MB: -0.2° rms : 15°
SWIM partition matched to MFWAM wind-wave	0.89x - 0.20 CC: 0.94 MB: -0.43 m rms : 0.29 m SI: 17%	0.87x+19 CC: 0.83 MB: 9.2 m rms : 23 m SI: 26%	0.96x+8.0 CC: 0.98 MB: -0.6° rms : 16°

Each cell gives the linear regression, the correlation coefficient (CC), the mean bias (MB), the rms difference, the scatter index (SI)- except for the direction in this latter case). Number of points is 105024 (data from 26th April to 8th May 2019). See text for other details.

($H_s > 3$ m) [see Fig. 18(a)]. For the 13-day period analyzed here, most of the overestimated H_s values are located in the Southern part of the oceans, in the region of high wind speed and high significant wave height. Very similar results were obtained in terms of bias for beams 6° and 8°, but with a slightly larger rms difference (2%–4% increase). For the direction, the agreement is good except in the direction interval [170°–195°] from North and its 180° modulo counterpart [see also Fig. 18(b)]. We verified that this is due to limitations in the detection of waves propagating in the along-track direction, which occur in spite of our noise correction improvement. For the dominant wavelength, a high correlation coefficient is observed, however, slightly less than in the case of H_s . Fig. 18(c) indicates that peak wavelengths as short as 70 m are detected on the SWIM spectra, a threshold which is compliant with our initial specifications. The few outliers shown in Fig. 18(c) correspond to SWIM wavelengths underestimated with respect to MFWAM, when the MFWAM wavelengths are larger than about 250 m. Most of these points are associated with along-track wave propagating waves, which are also identified as outliers in Fig. 18(b). Overall, the same conclusions were reached on these three parameters with data from SWIM beams 8° and 6°. However, an increased effect of the above-mentioned limitations is noted for observations from the 6° beam. This is likely due to a higher impact of speckle at this incidence with respect to the other beams.

2) *Analysis of Wave Parameters From Partitions*: Analyzing parameters from wave partitions is important because these parameters are those used in the assimilation of wave spectral observations for wave models [27]. This is also the information required to study the spatiotemporal evolution of wave fields

with an approach as the one proposed by Collard *et al.* [28]. For the objective of SWIM data validation, considering partitions instead of the full spectrum is a way to better focus the analysis on the parameters of different wave systems. It also minimizes the possible contribution of the background noise, because the contours of partitions exclude a large part of the noise floor. On the other hand, comparing parameters of wave partitions requires to adequately associate wave partitions from the two sets. In the first step, we associated the most energetic partition of SWIM spectra (called the 1st SWIM partition) to the most energetic swell detected by MFWAM (called the 1st swell from MFWAM). In both cases, partitioning was carried out by using the classical watershed algorithm [25], but for SWIM spectra, we did not use any additional assumption to classify the partitions as swell or wind sea. In contrast, partitions identified in output of the MFWAM model are classified into two swell systems and one wind-wave system. For this latter category, a criterion on wave age is used based on the ratio of U/C_p , where U is the wind speed of the model and C_p the phase velocity of the partition wavelength projected in the wind direction. We verified that in the analyzed data set, the 1st swell partition of MFWAM is the most energetic one among the three MFWAM partitions for 80% of the cases, and thus, in 80% of the cases, the simple SWIM/MFWAM association of partitions as described just above is fully justified. Comparisons on wave parameters are illustrated in Fig. 19 and the scores are given in the second line of Table VIII. In addition, geographical maps of the same parameters are illustrated in Fig. 20. Although the statistical parameters indicate generally lower scores with respect to the comparison carried out for the full spectra parameters, we still observe a rather good consistency between the SWIM and MFWAM parameters. For the wave heights of the 1st SWIM partition compared to the 1st swell of MFWAM, we find the same trend as in Fig. 18, with an overestimation of SWIM with respect to MFWAM for the smallest wave heights (<1.5 m) and an underestimation for the largest ones. Underestimation of the SWIM partition energy with respect to MFWAM occurs in the southern hemisphere, in the region of high H_s [Fig. 20(a) and (d)]. The results are similar for beams 6° and 8° with, however, a slightly larger dispersion (rms 0.48 and 0.49 m, respectively, compared to 0.40 m for beam 10°). As for the direction, the global scores are clearly impacted by inconsistent wave directions found in the sector [170°–195°] from North (modulo 180°) which are the directions corresponding roughly to the along-track directions [see also Fig. 20(c) and (f)]. But outside this interval, the correspondence between the SWIM and MFWAM directions is excellent with almost no bias. For the wavelengths [Fig. 19(c)], the bias remains small (less than 30 m) at all wavelengths but we also observe two groups of outliers. The first one, for SWIM wavelengths between 60 and 120 m, corresponds to the along-track propagating waves (see also Fig. 20). The outliers are probably related to an incorrect association between partitions in this case. The second one with overestimated wavelengths when the MFWAM values are around 100 m. The reason for this cloud of outliers is not very clear yet, but it may be partially due to the presence of some

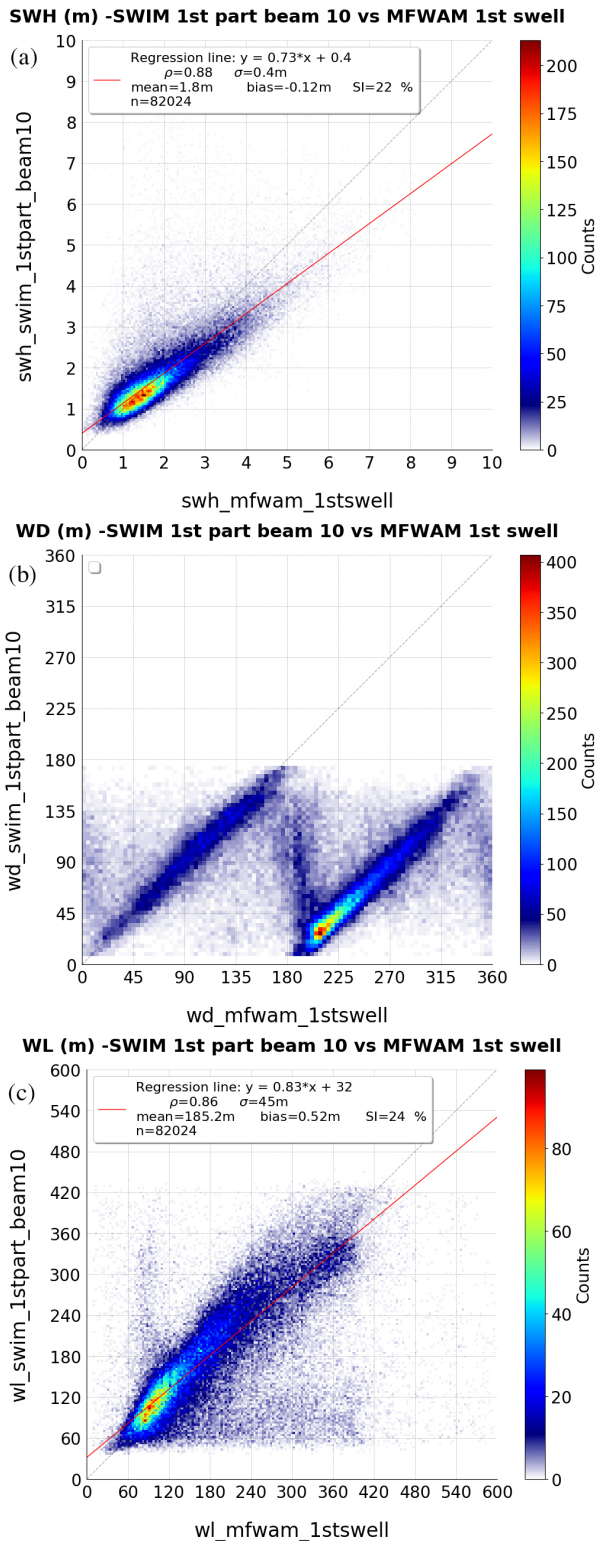


Fig. 19. Same as Fig. 18 but for the parameters of the 1st partition if the SWIM spectra (beam 10°) compared to the parameters of the 1st swell of MFWAM. (a) Significant wave height H_s . (b) Dominant direction (from North). (c) Dominant wavelength. The color code represents the number of points per bin of values. The red line on (a) and (c) represents the linear fit.

parasitic peaks in the wave spectra (see also Section VIII-B) which are not well filtered at the present stage (for the validation phase, no rejection of data based on a criterion on nonhomogeneous scenes was applied).

In spite of these difficulties, we can conclude on an overall good assessment for the parameters of the first SWIM partitions: the statistics indicate that 56% of samples exhibit a difference in wave height smaller than ± 30 cm, 69% with a difference less than ± 32 m in wavelength, and 78% with difference in direction less than $\pm 25^\circ$.

In the second step, the parameters of the SWIM and MFWAM partitions were analyzed by imposing a cross-assignment between the SWIM and MFWAM partitions. This was carried out, by matching pairs of partitions which minimize the distance in the wavenumber space, as proposed in [26]. This somehow constrains the results on the direction and wavelength but not on the significant wave height. As expected, the results are quite good for the wavelengths and directions, significantly better than without cross-assignment of partitions as indicated by slopes of the regression line which are closer to 1, and smaller rms differences. The best results are for the wind-wave partitions of MFWAM matched to a SWIM partition, with the slope of the regression close to unity and rms differences of ~ 27 m for the wavelength and $\sim 16^\circ$ for the direction. For the wave heights, the main result is that the underestimation of SWIM significant wave height above 1.5–2 m still remains when the partitions are matched. So this confirms the trend found with the full spectra and with the first approach of partition analysis.

We also analyzed the partitions parameters cross-assigned by their wave height values. By doing this, the results on wavelength and direction are not constrained. In this case, the results (not illustrated here) are very close to those of the first step (without cross-assignment) with in particular, the same outlier population on wavelength and direction. This confirms that these outliers are mainly due to misassociation between partitions. Part of this misassociation is due to the limit of SWIM detection in the along-track direction and another part to a different ranking of partitions between SWIM and MFWAM. This test also showed that even with a constraint applied on wave height when associating the SWIM and MFWAM partitions, we find an underestimate of SWIM H_s at small wave height and overestimate at large H_s (regression line $0.78x + 0.24$).

Finally, in a third step, we compared wave parameters estimated on fully matched partitions. In this case, the partitions were *a posteriori* calculated on the symmetrized MFWAM spectra and overlaid on SWIM spectra. Parameters of the new SWIM partitions were then calculated with the same partition contours as in the case of the MFWAM spectra. As this approach strongly constrains the wavelengths and directions, we only used this approach in complementary to the other comparisons, in particular to discuss the relative scores between SWIM beams and between partitions. Tables IX–XI give the results of this analysis. The first comment is that the parameters from beam 10° give the best agreement with the MFWAM compared to the cases from the other SWIM beams. This is true for all parameters and all statistical indicators (the mean bias, rms difference, and scatter index). The reason is probably twofold: the beam 10° is the less sensitive to possible wind fluctuations within the footprint, and it is associated with the smallest speckle noise perturbation. The mean bias on

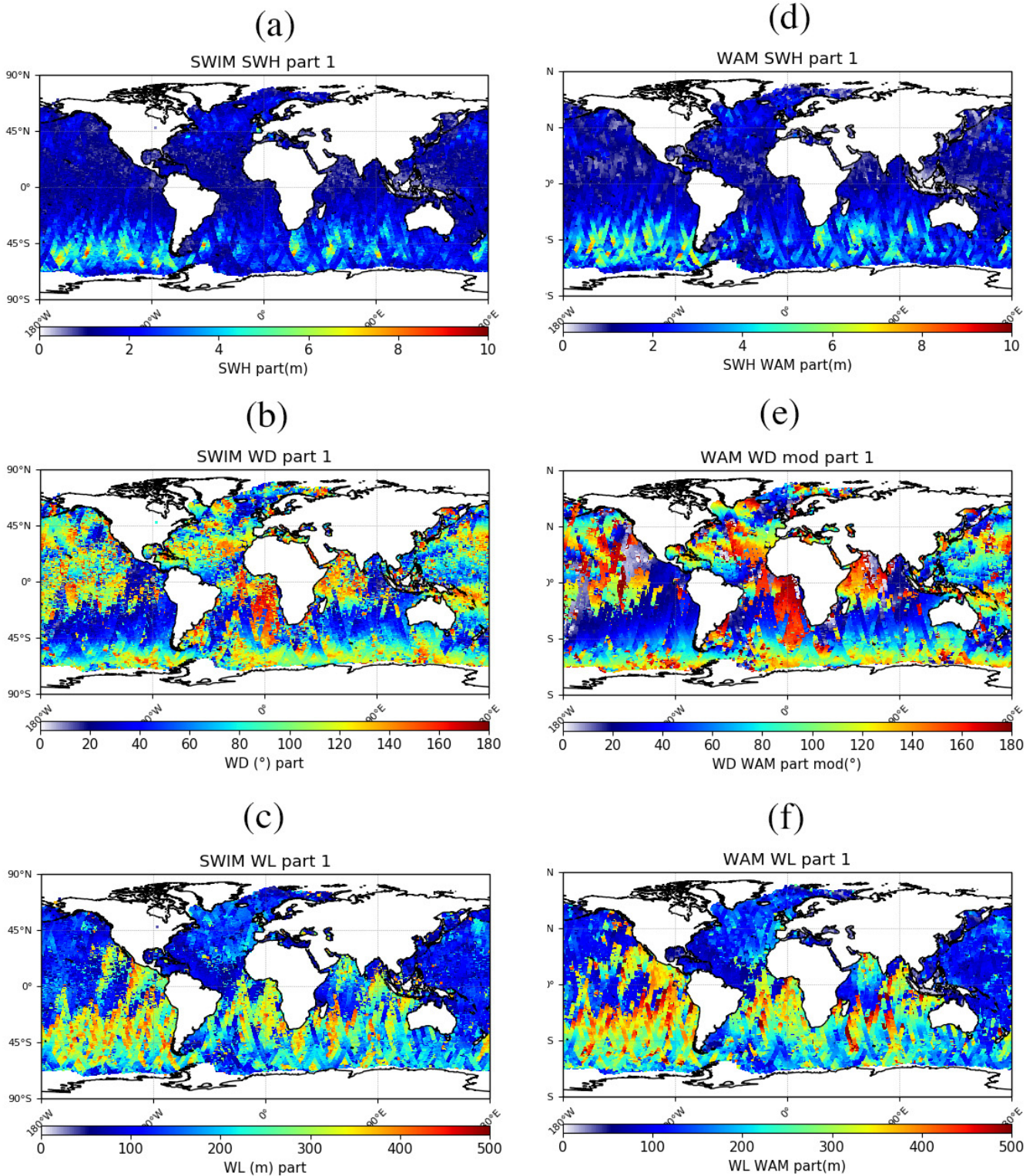


Fig. 20. Maps of (a)–(c) SWIM and (d)–(f) MFWAM parameters for a period of about 13 days starting on April 26, 2019, 02:00. (a) and (d) Wave height of the first partition. (b) and (e) Direction of the first partition (for MFWAM, the directions have been folded in the $[0^\circ\text{--}180^\circ]$ interval to be compared with the SWIM data). (c) and (f) Wavelength of the first partition. The SWIM results are shown for the 10° incidence beam. See text for details.

H_s has as similar order of magnitude for the three beams (0.21–0.31 m when considering all the partitions). This results from a small positive bias of SWIM with respect to MFWAM for $H_s \sim < 3$ m and negative bias at larger H_s . For beam 10° ,

for example, the mean relative bias is between 14% and 2% for H_s between 1.5 and 3 m but is only 4% for H_s of 6 m. Almost similar biases are obtained for the other beams, indicating that the speckle correction compensates adequately the differences

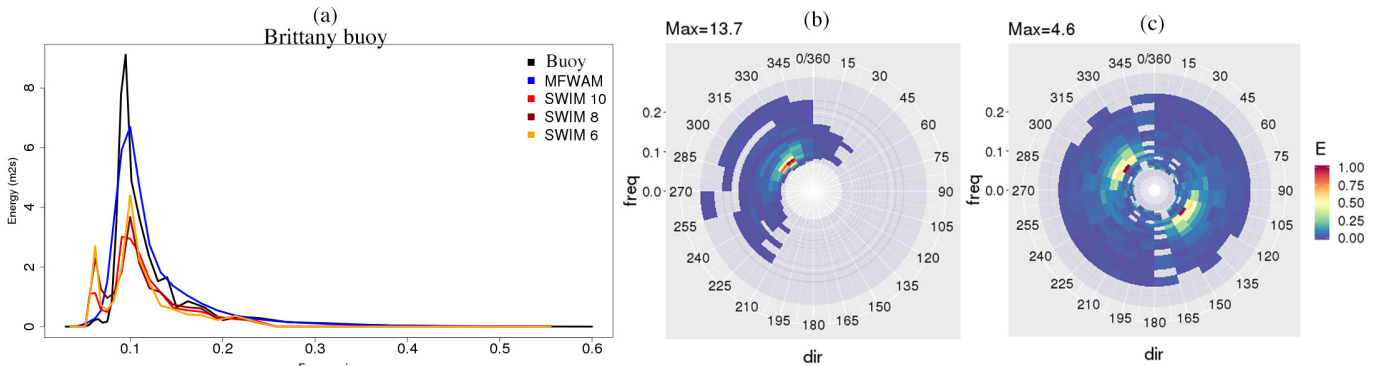


Fig. 21. (a) Omnidirectional spectra (m^2/s) from the Brittany buoy ($47^\circ 33' 0''$ N, $8^\circ 28' 12''$ W), MFWAM, and SWIM (three beams with the red, brown, and yellow curves as indicated in the insert) on August 19, 2019, 18:00 UTC. Directional spectrum from (b) buoy and (c) SWIM beam 10° . In (b) and (c), the color scale is relative to the maximum of energy of each plot.

in the noise levels evidenced in the data (Section VII). The rms difference on H_s is the smallest for beam 10° (0.41 m when considering all partitions) and the largest for beam 6° (0.58 m when considering all partitions). For a given SWIM beam, it decreases with the rank of the partition, but this is probably due to the range of H_s values encountered for each partition ([0–10], [0–6], and [0–4] m for the 1st, 2nd, and 3rd partitions, respectively). As for the direction, the mean bias is less than 1° (a good correspondence was expected because the partitions are forced to the same contours), while the rms difference is between 19° (beam 10° considering all partitions) and 26° (beam 6° , considering all partitions). This is slightly more, although still comparable, at least for beam 10° , with the initial goal which was specified to 15° . Finally, for the wavelength of the partitions, the rms difference is between 58 m (beam 10° , 1st partition) and 76 m (beam 6° , 2nd partition). The scatter plots (not shown) indicate that this relatively large rms difference is due to some outliers, with SWIM wavelengths spanning over the 200–500-m range, while the MFWAM values are less than about 200 m. This is similar to what was illustrated in Fig. 19(c) and named “second region of outliers.” The scatter plot also confirms that the other region of outliers identified in Fig. 19(c) does not exist when the partitions are imposed with the same contours as in MFWAM. This confirms our comment on Fig. 19(c) in which we attributed these outliers to misassociation between partitions.

Overall, all the results obtained with our statistical analysis (several approaches) indicate that the best agreements of SWIM parameters with respect to MFWAM are found for the 10° beam. They also show that a very good estimation of the direction is obtained when errors in cross-assignment are minimized (almost no biases, rms 15° – 20° for the beam 10°) but the quality is degraded for waves propagating close to the along-track direction in spite of the proposed *ad hoc* treatment of speckle noise. Similarly, biases on wavelengths are generally small, and the rms values are of the order of magnitude of 30–75 m depending on the approach used. The limitations in the detection of waves propagating close to the along-track direction and/or the presence of parasitic peaks in the SWIM spectra may explain a large part of these rms values on wavelengths.

B. Three Case Studies

In this section, we present three specific studies. The first two illustrate comparisons between wave spectra or wave parameters from SWIM and *in situ* measurements (complemented by the MFWAM model and/or SAR data).

The third one corresponds to an analysis of wave evolution in a fetch limited case.

1) Comparison of SWIM, Buoy, and Model Wave Spectra:

In this case, buoy measurements are compared to SWIM spectra converted into wave height spectra as a function of frequency, taking into account the dispersion relation in deep water. We discuss here two situations, the first one (case 1) corresponding to a young swell system and the second one (case 2) to a mixed sea condition.

For case 1, the comparison is carried out at the location of the Brittany buoy data ($47^\circ 33' 0''$ N $8^\circ 28' 12''$ W) on August 19, 2019, 18:00 UTC). This case corresponds to a young swell with $H_s \sim 2$ m from NW generated in the Atlantic open ocean. Fig. 21 compares the 1-D and 2-D spectra from the Brittany buoy, the SWIM data, and the MFWAM model. The peak and shape of the 1-D spectrum from SWIM are in good agreement with the buoy and the model. However, the SWIM data show two shortcomings: the energy is underestimated in the swell energy part, and there is a parasitic peak at low frequency. The underestimation of energy or wave height is compatible with the statistical analysis discussed in Section VIII-B. The parasitic peak (corresponding to wavelengths close to the 500-m wavelength limit) is probably due to one of these two factors: either lack of homogeneity over the SWIM footprint, which induces energy at low wavenumber, or remaining presence of noise floor of the slope spectra which is significantly amplified at these wavelengths when converting to wave height spectra. These two perturbations will be studied in more detail in the future, and improvements are expected by applying additional quality controls, in particular to identify and reject nonhomogeneous scenes (work under progress). Note that on the other hand, the good consistency in the shape of the spectra with frequency is an indirect indication that the linear MTF is appropriate.

The second case corresponds to a mixed sea condition generated by a midlatitude storm in the Atlantic waters. According to the buoy observations, there is first a wind

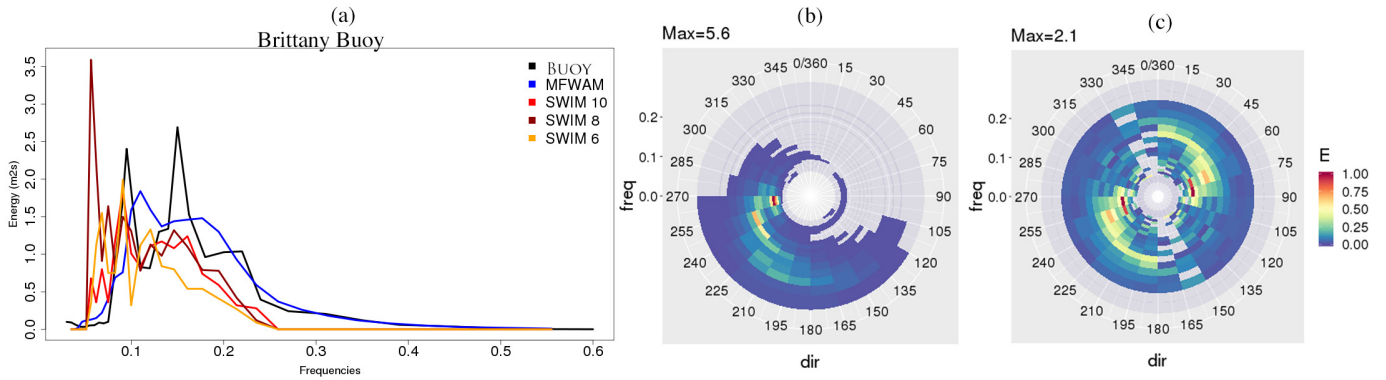


Fig. 22. (a) Omnidirectional spectra (m^2/s) from the Brittany buoy ($47^\circ 33' 0''$ N, $8^\circ 28' 12''$ W), MFWAM, and SWIM (three beams with the red, brown, and yellow curves as indicated in the insert) on July 24, 2019, 18:00 UTC. Directional spectrum from (b) buoy and (c) SWIM beam 10° . In (b) and (c), the color scale is relative to the maximum of energy of each plot.

sea from South with a 0.2-Hz peak frequency. As shown in Fig. 22, the main part of this component is captured by SWIM, although its energy seems underestimated.

The correspondence with respect to the buoy is much better for SWIM spectra obtained with the beams at 8° and 10° incidence than with the beam at 6° . There are also two swell systems, one around 0.16 Hz and one around 0.09 Hz. Both swell systems are well identified by SWIM which better captures the second swell from West than the model. As observed for the previous case, there is also an important parasitic peak at low frequency compared to the buoy and MFWAM spectra.

2) *Time Series of Wave Parameters in the Pacific Ocean:* The second illustration deals with comparisons of the SWIM data with *in situ* measurements located close to the island of Moorea in the South Pacific (-149.82° E, -17.61° N). The *in situ* wave parameters were obtained by analyzing 1-Hz time series of a pressure probe (OSSI probe) installed on the outer slope of the “Paroa” coral reef. CFOSAT data at a distance ranging from 25 to 300 km from the *in situ* probe are considered in this analysis. A comparison between the SWIM data and *in situ* data is reported in Fig. 23. It confirms that the local variations of H_s with time are well detected by SWIM. It is, however, fair to note that H_s values estimated from the off-nadir beams appear systematically slightly overestimated [Fig. 23(a)]. As for the dominant wavelength [Fig. 23(b)], there is a good agreement for all SWIM beams. SWIM captures very well the dominant wavelength variations with time, with changes from 100 to 500 m or vice versa observed over short time periods (of the order of a day).

3) *Interest of SWIM Observations for Studies of Wave Evolution at Regional Case:* The advantage of the multiangular and continuous sampling of the SWIM geometry of observation is illustrated for a situation of waves evolving under fetch limited conditions. These fetch-limited conditions are frequent in the North Mediterranean Sea under “Tramontane” or “Mistral” wind events which blow from the coast with a constant direction and almost constant wind speed from North or North–West. Such an event occurred during a CFOSAT passage, on April 29, 2019, with a wind from Northwest and a wind speed of about 11–14 m/s. The orientation of the satellite track with respect to the coast, and the sampling

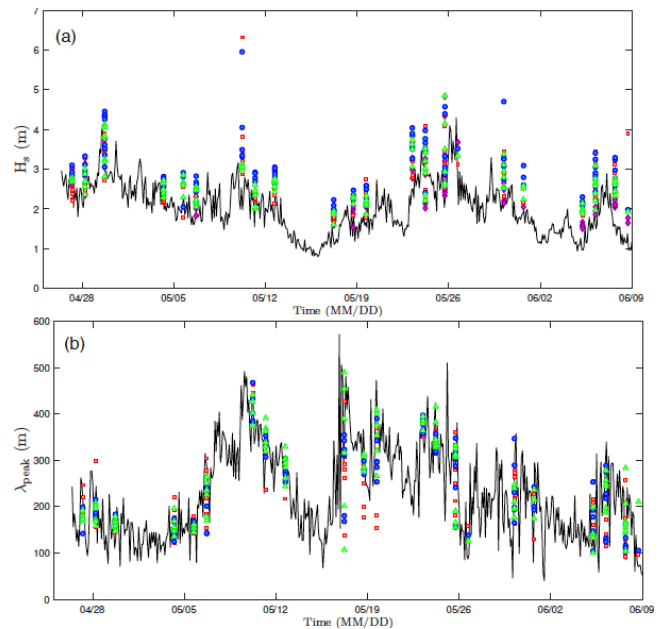


Fig. 23. Time series of (a) H_s in meters and (b) peak wavelength in meters from SWIM and OSSI probe in Moorea (-149.82° E, -17.61° N) between April 28, 2019, and June 9, 2019. The black curve indicates the *in situ* measurements. The CFOSAT nadir measurements are reported in magenta in (a). The CFOSAT 6° , 8° , and 10° beams are reported in red, blue, and green, respectively [(a) and (b)].

at different incidence angles with rotating geometry, allows to estimate wave spectra for multiple fetch distances with SWIM observations from the beams 4° , 6° , 8° , and 10° . For this specific study, the SWIM directional spectra were evaluated directly from the fluctuation spectra of the L1b product (no resampling in the wave box of L2 products) to analyze the evolution of the spectral peak wavenumber with the fetch distance. The results are shown in Fig. 24(a) where they are complemented by the same analysis performed on Sentinel-1b images (SAR in image mode) and compared to the WW3 model results. It shows that in this condition of almost constant wind along the fetch direction, and at fetches between 80 and 250 km, the peak wavenumber follows the expected Jonswap law [29] accounting for a wind speed of 11.5 m/s. After 250 km, the peak wavenumber stabilizes,

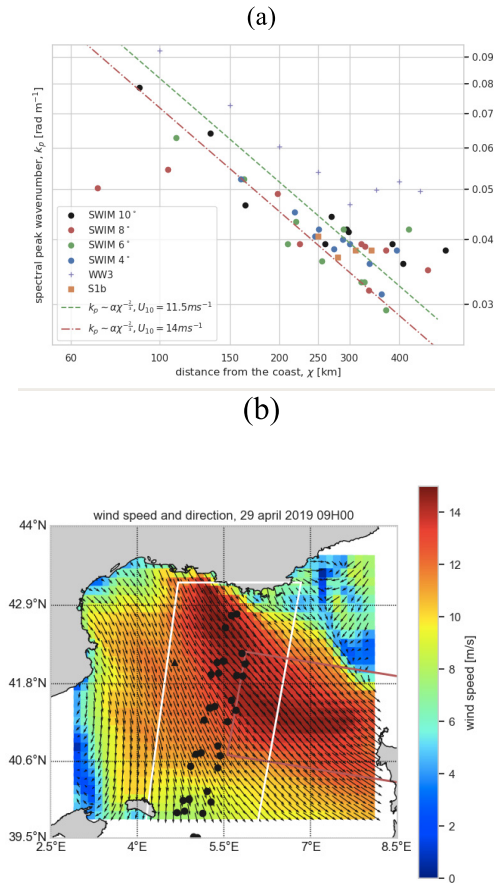


Fig. 24. Case of April 29, 2019, in the North Mediterranean sea. (a) Peak frequency as a function of the fetch [i.e., distance to the coast along the wind direction, see Fig. 24(b)] estimated from SWIM (color dots for SWIM beams 4°, 6°, 8°, and 10°), from S-1B SAR image (orange square symbols), and WW3 (plus signs). The two lines represent a fit of the wavenumber following a power law as a function of the distance of fetch using the SWIM and S-1B for a constant wind speed of 11.5 m/s (green dashed line) and 14 m/s (red dashed-dotted line). (b) Wind vector field and position of data sets. The SWIM 10° beam swath extension is shown with a white frame, black dots represent coordinates of the SWIM data used in Fig. 24(a), and Sentinel-1b image position is shown with a red frame.

reaching conditions of to fully developed wave conditions. It is remarkable to note that with the SWIM data it is possible to follow continuously the increase of the dominant wavelength from about 80 to 160 m over 170 km of fetch distance. The WW3 model results also follow this law but the peak wavenumbers are biased high with respect to the observations. This probably indicates some bias in the wind or stress forcing of WW3. This analysis of the presented data set illustrates the interest of SWIM for characterizing the spatial structure of a wave field at a regional scale. This is essential for wave model improvement and calibration.

IX. SYNTHESIS AND CONCLUSION

In this article, we have presented the first analysis of the geophysical products provided by the SWIM instrument on-board the CFOSAT.

We have first illustrated the good instrumental behavior of the instrument. Then, we have illustrated the high quality of data obtained from the nadir observations (significant wave

height, normalized radar cross section, and wind speed). Compared to the Jason-3 products, the performance on these parameters is of the same order in spite of a lower acquisition rate but thanks to the new “adaptive” retracking algorithm. We have shown the consistency of the normalized radar cross sections σ_0 for all incidence beams (except for the 2° beam which still needs to be assessed). Without any *a posteriori* calibration, the trend of σ_0 with incidence and with wind speed is very similar to that provided by the GPM data, and the bias with respect to the mean GPM values is less or of the order of 1 dB.

The Level 1b data include fluctuation of radar cross section, which are supposed to be maximum when the radar look direction is aligned with the wave propagation. The density spectra of these fluctuations have been compared to wave spectra from the WW3 model. We have found a good correlation for all wavenumbers of interest (1.25×10^{-2} to 8.98×10^{-2} rad \cdot m $^{-1}$) except in a sector of about $\pm 15^\circ$ around the direction of the satellite track. The best correlation is obtained for SWIM beams at 8° and 10° incidences. The decrease of correlation in the azimuthal sector aligned with the satellite track is attributed to the increase of noise due to the decrease of the radar Doppler bandwidth in this direction. An empirical model was built by analyzing the SWIM data themselves to parameterize the density spectrum of speckle both within and outside this perturbed angular sector. It was shown that within the angular sector affected by the decrease of radar Doppler bandwidth, the speckle intensity varies with latitude and with sea surface conditions. In contrast, for all other directions, for which the Doppler bandwidth is larger than the PRF, the speckle noise level is governed by the number of samples averaged in time and in radial distance.

Finally, the evaluation of the wave spectra and their main parameters (wave height dominant direction and dominant wavelength) was presented. The analysis performed by using the correlation index proposed by Hasselmann *et al.* [26] allows to conclude that the best (the lowest, respectively) consistency with model spectra is obtained for the 10° beam (6° beam, respectively) observations.

The quality of the wave parameters was assessed using two approaches: comparison of wave parameters from the SWIM and the MFWAM model spectra without partitioning and comparison of parameters of the SWIM and MFWAM spectral partitions. In this latter case, in order to reach conclusions not biased by the difference in partitions, we discussed three kinds of comparisons: 1) parameters from separate partition estimations (without cross-assignment); 2) parameters from the SWIM partitions matched to the MFWAM partitions obtained by minimizing the dominant wavenumber vector distance or the distance in wave height, and 3) parameters obtained by overlaying the MFWAM partitions on the SWIM spectra. Overall, the results indicate the following:

- 1) SWIM observations from beam 10° give the best results, while the beam 6° gives the less satisfactory results. This may be explained by the smallest sensitivity of σ_0 to wind speed close to the 10° incidence and by the smallest contribution of speckle contribution at this incidence (the largest number of the averaged echoes).

TABLE IX

STATISTICAL SCORES FOR THE COMPARISON OF THE SIGNIFICANT WAVE HEIGHT OF THE MFWAM WAVE SPECTRA PARTITIONS AND THE SWIM SPECTRA PARTITIONS WHEN THE PARTITIONS OF MFWAM ARE OVERLAID ON THE SWIM SPECTRA

Hs	Beam 6°	Beam 8°	Beam 10°
Nb of points	All : 570 498 part 1 : 250 130 part 2 : 197 381 part 3 : 122 987	All : 567 891 part 1 : 249 050 part 2 : 196 427 part 3 : 122 414	All : 556 333 part 1 : 243 736 part 2 : 192 482 part 3 : 120 115
Mean Bias [m]	All : 0,23 part 1 : 0,16 part 2 : 0,28 part 3 : 0,29	All : 0,31 part 1 : 0,30 part 2 : 0,33 part 3 : 0,30	All : 0,21 part 1 : 0,17 part 2 : 0,24 part 3 : 0,24
RMSE [m]	All : 0,58 part 1 : 0,71 part 2 : 0,50 part 3 : 0,39	All : 0,54 part 1 : 0,65 part 2 : 0,48 part 3 : 0,35	All : 0,41 part 1 : 0,49 part 2 : 0,34 part 3 : 0,29
Scatter Index	All : 40,3 part 1 : 30,4 part 2 : 51,4 part 3 : 84,8	All : 37,2 part 1 : 28,2 part 2 : 49,3 part 3 : 74,4	All : 27,9 part 1 : 21,2 part 2 : 34,5 part 3 : 62,7

THE DATA SET COVERS FROM APRIL 25, 2019, TO JUNE 9, 2019

- 2) The significant wave height is overestimated at wave heights smaller than 2–3m (depending on the method used for the comparison) and underestimated at larger wave heights. This shortcoming, probably due to remaining uncertainties in the noise correction and in the MTF estimation, may be minimized in the future by applying an empirical correction on significant wave heights or by normalizing the spectra with the nadir observation as reference. As for the dispersion, the comparisons with model data indicate an rms difference of 0.26–0.71 m depending on the SWIM beam and method used for the evaluation. The rms difference is significantly less for the beam 10° compared to the other beams and for the full spectrum and first partition, indicating that when a good accuracy is required on wave height, it is preferable to focus on the 10° beam full spectrum or 1st partition data.
- 3) The direction of the waves is generally well retrieved except in some of the conditions where waves propagate in the along-track sector (there are larger limitations for long swell cases in this case). The best consistency with model and *in situ* data is for the beam 10° and the least one with the beam 6°. The rms differences with respect to the same reference (the MFWAM model) are of the order of 15°–29° depending on the method of analysis.
- 4) The dominant wavelengths, as identified on the wave slope spectra, are also well retrieved except in the along-track directions and mainly for the long swell. Again, the best results are for the beam 10° and the first SWIM partition. The order of magnitude of the rms differences with respect to the model is typically of 30–40 m.

First comparisons with *in situ* observations confirm the main characteristics obtained with the statistical analysis. For some cases, a parasitic peak at low wavenumber is identified in the

TABLE X

SAME AS TABLE IX BUT FOR THE DIRECTION OF THE PARTITIONS

Dir	Beam 6°	Beam 8°	Beam 10°
Mean Bias [deg.]	All : -0,4 part 1 : -0,8 part 2 : 0,0 part 3 : -0,2	All : -0,5 part 1 : -0,9 part 2 : -0,1 part 3 : -0,2	All : -0,5 part 1 : -0,6 part 2 : -0,3 part 3 : -0,4
RMSE [deg.]	All : 26,4 part 1 : 29,0 part 2 : 26,0 part 3 : 21,4	All : 23,4 part 1 : 24,8 part 2 : 23,5 part 3 : 20,3	All : 19,2 part 1 : 19,3 part 2 : 19,5 part 3 : 18,4

TABLE XI

SAME AS TABLE IX BUT FOR THE WAVELENGTH OF THE PARTITIONS

Wl	Beam 6°	Beam 8°	Beam 10°
Mean Bias [m]	All : 13,9 part 1 : 11,4 part 2 : 14,4 part 3 : 18,4	All : 8,3 part 1 : 3,9 part 2 : 9,4 part 3 : 15,6	All : 5,6 part 1 : 0,2 part 2 : 7,0 part 3 : 14,3
RMSE [m]	All : 73,5 part 1 : 73,8 part 2 : 75,6 part 3 : 69,3	All : 67,3 part 1 : 65,5 part 2 : 70,2 part 3 : 65,3	All : 62 part 1 : 57,9 part 2 : 66,0 part 3 : 62,5
Scatter Index	All : 35,6 part 1 : 39,7 part 2 : 36,9 part 3 : 27,5	All : 32,5 part 1 : 35,2 part 2 : 34,3 part 3 : 25,9	All : 30,0 part 1 : 31,1 part 2 : 32,2 part 3 : 24,8

spectra. It is likely due to an amplification of the noise floor when converting slope spectra to height spectra.

Overall, the analysis presented in this article shows that SWIM is able to provide the spectral properties of ocean waves in the wavelength range [70–500 m]. Although no detailed quality control was applied at this stage (like removing scenes affected by rain or nonhomogeneous conditions), we showed that SWIM products already bring valuable information on wave spectra details and wave parameters which are very complementary to *in situ* observations, other satellite observations, or models. In particular, the evolution of spectral properties at the regional scale seems very promising, even in coastal conditions.

Further improvements on the wave products are expected with the planned introduction of quality controls (rejection of nonhomogeneous wind or wave scenes, scenes impacted by rain, etc.), better filtering of the energy of low wavenumbers, and refinement of the MTF. In addition, downstream of the inversion, wave partitions as determined from the operational algorithm will be more constrained in order to reject partitions with too low energy or to merge partitions which are close in direction. Work is under progress to assess these new improvements and will be reported in future articles. Also, more extensive comparisons with *in situ* data will be carried out, in particular using the National Oceanic and Atmospheric Administration (NOAA) buoy network. This requires, however, to reprocess the SWIM data according to the improvements presented in this article over a long period of time to allow for a large comparison data set.

ACKNOWLEDGMENT

The authors are very grateful to the reviewers for their helpful comments and encouragements. They wish to acknowledge the major role of the colleagues who contributed to the success of the mission and instrument performance. In particular, P. Castillan and J.-M. Lachiver as project SWIM managers in the development and operational phase, respectively, N. Corcoral as System Engineer, and T. Amiot as SWIM instrument responsible. They have a thought for G. Boutonnet, the former Project Manager of the French ground segment, who left us prematurely. Surface Waves Investigation and Monitoring (SWIM) was built by Thales Alenia Space Industry (TAS) under a Centre National d'Etudes Spatiales (CNES) contract. They thank L. Rey and B. Carrayon from TAS for their role in the SWIM design, realization, and tests. F. Nouguier, LOPS, Plouzané, France, and F. Collard, Océanodatalab, Locmaria-Plouzané, France, helped to interpret the fluctuation spectra and speckle behavior, thanks to their numerical approaches. Comparisons with *in situ* data in the Pacific Ocean were carried out, thanks to the contribution of F. Zuberer at CRIOBE, Perpignan, France, for the *in situ* measurements. They also thank B. Perret at Collecte Localisation Satellite (CLS), Ramonville Saint-Agne, France, C. Dufour at Laboratoire Atmosphère, Milieux, Observations Spatiales (LATMOS), Guyancourt, France, who developed the main part of the computer architecture, data bases, and software used for the data analysis presented here. All China France Oceanography Satellite (CFOSAT) products are provided by courtesy of Chinese National Space Agency (CNSA) and CNES.

REFERENCES

- [1] D. Hauser, D. Xiaolong, L. Aouf, C. Tison, and P. Castillan, "Overview of the CFOSAT mission," in *Proc. IEEE Int. Geosci. Remote Sens. Symp. (IGARSS)*, Beijing, China, Jul. 2016, pp. 5789–5792.
- [2] D. Hauser, C. Tison, T. Amiot, L. Delaye, N. Corcoral, and P. Castillan, "SWIM: The first spaceborne wave scatterometer," *IEEE Trans. Geosci. Remote Sens.*, vol. 55, no. 5, pp. 3000–3014, May 2017, doi: [10.1109/TGRS.2017.2658672](https://doi.org/10.1109/TGRS.2017.2658672).
- [3] W. Alpers and C. Bruening, "On the relative importance of motion-related contributions to the SAR imaging mechanism of ocean surface waves," *IEEE Trans. Geosci. Remote Sens.*, vol. GE-24, no. 6, pp. 873–885, Nov. 1986.
- [4] H. Li, B. Chapron, A. Mouche, and J. E. Stopa, "A new ocean SAR cross-spectral parameter: Definition and directional property using the global Sentinel-1 measurements," *J. Geophys. Res., Oceans*, vol. 124, no. 3, pp. 1566–1577, Mar. 2019, doi: [10.1029/2018JC014638](https://doi.org/10.1029/2018JC014638).
- [5] X. Dong, D. Zhu, W. Lin, H. Liu, and J. Jiang, "A Ku-band rotating fan-beam scatterometer: Design and performance simulations," in *Proc. IEEE Int. Geosci. Remote Sens. Symp.*, Jul. 2010, pp. 1081–1084.
- [6] F. C. Jackson, W. T. Walton, and P. L. Baker, "Aircraft and satellite measurement of ocean wave directional spectra using scanning-beam microwave radars," *J. Geophys. Res.*, vol. 90, no. C1, p. 987, 1985.
- [7] F. C. Jackson, W. T. Walton, and C. Y. Peng, "A comparison of *in situ* and airborne radar observations of ocean wave directionality," *J. Geophys. Res.*, vol. 90, no. C1, p. 1005, 1985.
- [8] D. Hauser, G. Caudal, G.-J. Rijckenberg, D. Vidal-Madjar, G. Laurent, and P. Lancelin, "RESSAC: A new airborne FM/CW radar ocean wave spectrometer," *IEEE Trans. Geosci. Remote Sens.*, vol. 30, no. 5, pp. 981–995, Sep. 1992.
- [9] G. Caudal, D. Hauser, R. Valentin, and C. Le Gac, "KuROS: A new airborne Ku-band Doppler radar for observation of surfaces," *J. Atmos. Ocean. Technol.*, vol. 31, no. 10, pp. 2223–2245, 2014.
- [10] F. C. Jackson, "Directional spectra from the radar ocean wave spectrometer during LEWEX," in *Directional Ocean Wave Spectra*, R. Beal, Ed. Baltimore, MD, USA: Johns Hopkins Univ. Press, 1991, pp. 91–97.
- [11] D. Vandemark, F. C. Jackson, E. J. Walsh, and B. Chapron, "Airborne radar measurements of ocean wave spectra and wind speed during the grand banks ERS-1 SAR wave experiment," *Atmos.-Ocean*, vol. 32, no. 1, pp. 143–178, Mar. 1994, doi: [10.1080/07055900.1994.9649493](https://doi.org/10.1080/07055900.1994.9649493).
- [12] B. Legresy, F. Papa, F. Remy, G. Vinay, M. van den Bosch, and O.-Z. Zanife, "ENVISAT radar altimeter measurements over continental surfaces and ice caps using the ICE-2 retracking algorithm," *Remote Sens. Environ.*, vol. 95, no. 2, pp. 150–163, Mar. 2005.
- [13] F. Ardhuin *et al.*, "Semiempirical dissipation source functions for ocean waves. Part I: Definition, calibration, and validation," *J. Phys. Oceanogr.*, vol. 40, no. 9, pp. 1917–1941, Sep. 2010, doi: [10.1175/2010JPO4324.1](https://doi.org/10.1175/2010JPO4324.1).
- [14] L. Aouf. (2018). CMEMS quality information document for global ocean waves analysis and forecasting product. CMEMS-GLO-QUID-001_027. [Online]. Available: <http://resources.marine.copernicus.eu/documents/QUID/CMEMS-GLO-QUID-001-027.pdf>
- [15] V. Gressani, F. Nouguier, and A. Mouche, "Wave spectrometer tilt modulation transfert function using near-nadir Ku- and Ka-band GPM radar measurements," in *Proc. IEEE Int. Geosci. Remote Sens. Symp. (IGARSS)*, Valencia, Spain, Jul. 2018, pp. 4107–4110.
- [16] G. Brown, "The average impulse response of a rough surface and its applications," *IEEE Trans. Antennas Propag.*, vol. AP-25, no. 1, pp. 67–74, Jan. 1977.
- [17] C. Tourain *et al.*, "CFOSAT SWIM adaptive retracking: Description and validation," *IEEE Trans. Geosci. Remote Sens.*, to be published.
- [18] J. A. Nelder and R. Mead, "A simplex method for function minimization," *Comput. J.*, vol. 7, no. 4, pp. 308–313, 1965, doi: [10.1093/7.4.308](https://doi.org/10.1093/7.4.308).
- [19] J. Gourrion *et al.*, "A two-parameter wind speed algorithm for Ku-band altimeters," *J. Atmos. Ocean. Technol.*, vol. 19, no. 12, pp. 2030–2048, 2002, doi: [10.1175/1520-0426.2002](https://doi.org/10.1175/1520-0426.2002).
- [20] F. Collard, "Algorithmes de vent et période moyenne des vagues JASON base de réseaux de neurones," Boost Technol., Bedford, NH, USA, Tech. Rep. BO-021-CLS-0407-RF, 2005, p. 33.
- [21] J. Tournadre, J. C. Poisson, N. Steunou, and B. Picard, "Validation of AltiKa matching pursuit rain flag," *Mar. Geodesy*, vol. 38, no. 1, pp. 107–123, 2015, doi: [10.1080/01490419.2014.1001048](https://doi.org/10.1080/01490419.2014.1001048).
- [22] F. T. Ulaby and D. G. Long, *Microwave Radar and Radiometric Remote Sensing*. Ann Arbor, MI, USA: Univ. Michigan Press, 2014.
- [23] J. F. R. Gower, "'Layover' in satellite radar images of ocean waves," *J. Geophys. Res.*, vol. 88, no. C12, p. 7719, 1983.
- [24] O. Boïso, L. Amarouche, J.-C. Lalaurie, and C.-A. Guerin, "Dynamical properties of sea surface microwave backscatter at low-incidence: Correlation time and Doppler shift," *IEEE Trans. Geosci. Remote Sens.*, vol. 54, no. 12, pp. 7385–7395, Dec. 2016, doi: [10.1109/TGRS.2016.2601242](https://doi.org/10.1109/TGRS.2016.2601242).
- [25] J. L. Hanson and O. M. Phillips, "Automated analysis of ocean surface directional wave spectra," *J. Atmos. Ocean. Technol.*, vol. 18, no. 2, pp. 277–293, Feb. 2001.
- [26] S. Hasselmann, C. Brüning, K. Hasselmann, and P. Heimbach, "An improved algorithm for the retrieval of ocean wave spectra from synthetic aperture radar image spectra," *J. Geophys. Res., Oceans*, vol. 101, no. C7, pp. 16615–16629, Jul. 1996.
- [27] L. Aouf *et al.*, "On the assimilation of CFOSAT wave data in the wave model MFWAM: Verification phase," in *Proc. IEEE Int. Geosci. Remote Sens. Symp. (IGARSS)*, Yokohama, Japan, Jul./Aug. 2019, pp. 7959–7961.
- [28] C. F. Collard, F. Ardhuin, and B. Chapron, "Monitoring and analysis of ocean swell fields from space: New methods for routine observations," *J. Geophys. Res.*, vol. 114, Jul. 2009, Art. no. C07023, doi: [10.1029/2008JC005215](https://doi.org/10.1029/2008JC005215).
- [29] K. Hasselmann *et al.*, "Measurements of wind-wave growth and swell decay during the Joint North Sea Wave Project (JONSWAP)," *Deut. Hydrogr. Z.*, vol. 8, pp. 1–95, Jan. 1973.



Danièle Hauser (Member, IEEE) received the Ph.D. thesis in meteorology in 1980 and a State thesis in physics in 1989.

She is currently a Senior Scientist with the Centre National de la Recherche Scientifique (CNRS), Guyancourt, France, and develops her research activity with the Laboratoire Atmosphère, Milieux, Observations Spatiales (LATMOS), Guyancourt. She is currently working on microwave observations of the ocean surface (surface wind, waves, and salinity) and air/sea interaction studies, for more than 25 years. She is currently a Principal Investigator of the China France Oceanography Satellite (CFOSAT) Mission dedicated to the global measurement of wind and waves from satellite.



Cédric Tourain received the one-year postgraduate degree in space technology from the Université de Méditerranée Aix-Marseille II, Marseille, France, in 2000 and the advance master's degree in aerospace mechanics and propulsion from the École Nationale Supérieure de l'Aéronautique et de l'Espace, Toulouse, France, in 2001.

He first worked on Flight Dynamics System with the Space Department, Thales Services, Toulouse. He moved to DORIS system exploitation in 2005, first as a System Integrity Manager with Collecte Localisation Satellite (CLS), Ramonville Saint-Agne, France, and then as a DORIS Exploitation Expert with the Centre National d'Études Spatiales (CNES, the French Space Agency), Toulouse, in 2009. In 2015, he moved to the China France Oceanography Satellite (CFOSAT) Project with the Radar Processing and Products Department, CNES. He coordinates CFOSAT products' processing definition and validation, and since 2019, he has been the CNES CFOSAT Project Scientist.



Laura Hermozo received the Engineering degree from the École Nationale Supérieure d'Électrotechnique, Électronique, Informatique, Hydraulique et des Télécommunications, Toulouse, France, in 2013 and the Ph.D. degree from the Collecte Localisation Satellites (CLS), Ramonville Saint-Agne, France/Centre National d'Études Spatiales (CNES, the French Space Agency), Toulouse, collaboration on the use of passive microwave observations for atmospheric water vapor estimations, in 2018.

She integrated the Radar Instrument and Performance Department, CNES. Since then, she has been involved in the China France Oceanography Satellite (CFOSAT) Project and is responsible for the definition and validation of the inversion algorithms at the instrument correction and calibration levels.

D. Alraddawi, photograph and biography not available at the time of publication.

L. Aouf, photograph and biography not available at the time of publication.

B. Chapron, photograph and biography not available at the time of publication.

A. Dalphinnet, photograph and biography not available at the time of publication.

L. Delaye, photograph and biography not available at the time of publication.

M. Dalila, photograph and biography not available at the time of publication.

E. Dormy, photograph and biography not available at the time of publication.

F. Gouillon, photograph and biography not available at the time of publication.

V. Gressani, photograph and biography not available at the time of publication.

A. Grouazel, photograph and biography not available at the time of publication.

G. Guitton, photograph and biography not available at the time of publication.

R. Husson, photograph and biography not available at the time of publication.

A. Mironov, photograph and biography not available at the time of publication.

A. Mouche, photograph and biography not available at the time of publication.

A. Ollivier, photograph and biography not available at the time of publication.

L. Oruba, photograph and biography not available at the time of publication.

F. Piras, photograph and biography not available at the time of publication.

R. Rodriguez Suquet, photograph and biography not available at the time of publication.

P. Schippers, photograph and biography not available at the time of publication.

C. Tison, photograph and biography not available at the time of publication.

Ngan Tran, photograph and biography not available at the time of publication.